Acta Astronautica 188 (2021) 334–351

Contents lists available at ScienceDirect

Acta Astronautica

journal homepage: www.elsevier.com/locate/actaastro

Research paper

Spacecraft relative navigation with an omnidirectional vision sensor

Omri Kaufman [a], Pini Gurfil [b,*]

[a] Autonomous Systems and Robotics Program, Technion, Haifa, 32000, Israel
[b] Faculty of Aerospace Engineering, Technion, Haifa, 32000, Israel

ARTICLE INFO

Keywords:
Omnidirectional vision sensor
Space navigation
Extended Kalman Filter
Computer vision
Spacecraft relative dynamics
Unified projection model

ABSTRACT

With the onset of autonomous spacecraft formation flying missions, the ability of satellites to autonomously navigate relatively to other space objects has become essential. To implement spacecraft relative navigation, relative measurements should be taken, and processed using relative state estimation. An efficient way to generate such information is by using vision-based measurements. Cameras are passive, low-energy, and information-rich sensors that do not actively interact with other space objects. However, pointing cameras with a conventional field-of-view to other space objects requires much a-priori initialization data; in particular, dedicated attitude maneuvers are needed, which may interfere with the satellite's main mission. One way to overcome these difficulties is to use an omnidirectional vision sensor, which has a 360-degree horizontal field of view. In this work, we present the development of an omnidirectional vision sensor for satellites, which can be used for spacecraft relative navigation, formation flying, and space situational awareness. The study includes the development of the measurement equations, dynamical models, and state estimation algorithms, as well as a numerical study, an experimental investigation, and a space scalability analysis.

1. Introduction

Autonomous spacecraft navigation relative to other space objects is becoming a common requirement in space missions. A distributed space system mission such as spacecraft formation flying [1] is an example of using several cooperating spacecraft, achieving mission redundancy, adaptability to variable conditions and the ability to replace a failing agent instead of the whole system.

Other missions require navigating relatively to non-cooperative objects. This includes on-orbit satellite servicing, where one of the spacecraft was not designed to be repaired or maintained in-orbit and, hence, it does not support interaction with the other vehicle. Space situational awareness is also an example in which a spacecraft is designed to avoid collisions with non-cooperative resident space objects such as space debris [2,3].

For the missions involving non-cooperative interactions, the aforementioned ability to navigate autonomously becomes more challenging. This is because there might be little or no *a priori* information about the structure or motion of the other object. Thus, an information-rich sensor will be useful. In addition, considering space conditions, in which energy efficiency is important, it is desired to use passive sensing. Therefore, solutions like 3-D laser-based sensors [4] may be infeasible, because they require considerable computational effort, and consume much energy. Thus, solutions such as vision-based sensors, which reconstruct the relative state by applying computer vision algorithms on passively acquired image pixels, are advantageous.

A single camera projects the 3-D environment onto 2-D, which yields partial state observability. To obtain the entire relative state, stereoscopic vision or N-ocular vision can be used [5,6]. Nevertheless, using a monocular vision sensor combined with a dynamical model, could lead to a sufficient reconstruction of the relative state. Additionally, in order to generate more information, a wide field of view (FOV) sensing is beneficial.

An omnidirectional vision sensor (ODVS), also referred to as panoramic catadioptric camera, provides a wide FOV. It enables sensing in 360 ° horizontally and about 45 °–80 ° vertically. Usually, it comprises of a mirror which is axially symmetric, an apparatus which supports the mirror, a lens and a camera.

The original idea of an omnidirectional camera was proposed by Rees [7], in a patent submitted to the US government in 1967. It used a hyperboloidal mirror in combination with a conventional imaging system for acquiring an omnidirectional image (ODI), which has a single center of projection. Later, Nayar and Baker [8,9] have geometrically analyzed the complete class of single-lens single-mirror catadioptric imaging systems, which satisfy the fixed viewpoint constraint (i.e. has a single center of projection), and developed an ideal omnidirectional vision sensor (ODVS) using a paraboloidal mirror and a telecentric

* Corresponding author.
E-mail addresses: omri.k@campus.technion.ac.il (O. Kaufman), pgurfil@technion.ac.il (P. Gurfil).

https://doi.org/10.1016/j.actaastro.2021.07.024
Received 27 January 2021; Received in revised form 23 May 2021; Accepted 16 July 2021
Available online 31 July 2021

lens. Nevertheless, using a hyperboloidal mirror shape as done by Svoboda [10], saves cost, and the added volume of an expensive telecentric lens.

ODVS are classified into four general types by their mirror shape: Conical Mirror - the easiest to manufacture, has a relatively small vertical viewing angle, lacking a single center of projection, and possesses large astigmatism; Spherical Mirror - superior for making small ODVS, has a large vertical viewing angle, lacking a single center of projection, which causes astigmatism that gradually eliminates as it gets near the ODI center; Paraboloidal Mirror - ideally realized with an expensive and large telecentric lens, which enables flexible mirror-lens distance design (since the projection is orthogonal to the vertical direction), has a single center of projection, with astigmatism that correlates to the size of the curvature; Hyperboloidal Mirror - challenging design (since the focal point of the hyperboloid needs to be set on the camera's focal point), can be combined with a normal lens, has a single center of projection, with astigmatism that correlates to the size of the curvature. In this work, an ODVS constructed of a hyperboloidal mirror and a close focusing lens (macro lens) was used. The motivation was to acquire a wide vertical viewing range with small astigmatism, using a smaller and less expensive system.

Using ODVS for navigation applications requires calibrating the sensor based on a nonlinear measurement model. Furthermore, inversion of the model can be used for initial state estimation. Puig compared different calibration methods based on different measurement models [11]. One of the main models is the spherical camera model which was used in this work. This model gives some calibration information about the constructed mirror and provides the theoretical projection function which enables inversion of the model; other models are based on distortion functions which are more complicated for inversion.

The *sphere* projection model, also called the *unified* projection model, was given by Geyer [12], and extended by Barreto [13]. Mei [14], expanded this model and added practical factors of radial and tangential distortions introduced by misalignment of telecentric lenses to the ideal theoretical model. This model is a compromise between a generic theory and over-parametrization, and is based on an exact theoretical projection function to which well-identified parameters are added, to model real-world errors.

An example for a different model is the simple model suggested by Svoboda et al. [15], wherein the projection of a space point onto the image plane can be modeled by a composition of two central projections. The first projects a space point onto the mirror, and the second projects the mirror point into the image. The geometry of various catadioptric cameras depends mostly on the first projection. The second projection is not as important, as long as it is a one-to-one mapping. If the first projection is a central projection, the catadioptric camera has the same mathematical model as any conventional perspective camera, and all the theories developed for conventional cameras can be used.

ODVS are used in a variety of applications such as robotics, autonomous vehicles, surveillance, navigation, and more. Tahri and Araujo simulated a catadioptric image-based visual servoing method for mobile robots [16]. Voigtländer et al. present methods for ball recognition and tracking using the catadioptric camera of a RoboCup robot [17]. Ehlgen et al. used catadioptric cameras to survey the surrounding area of vehicles [18]. Scaramuzza and Siegwart computed the ego-motion of a vehicle relative to the road using images from a single omnidirectional camera [19]. Rituerto et al. performed visual simultaneous localization and mapping (SLAM) with an omnidirectional camera [20]. Scotti et al. used an ODVS in conjunction with a pan–tilt zoom camera for surveillance [21]. Chahl and Srinivasan simulated 3D navigation based on panoramic imaging using an ODVS [22]. Lhuillier performed 3D reconstruction of indoor and outdoor scenes from a catadioptric image sequence [23]. Das et al. described a vision-based formation control framework and performed experiments of robot formation-keeping using ODVS [24].

Tracking a target captured by a vision sensor requires detecting and differentiating it from other targets first. This could be done by computer vision (CV) algorithms, processing the acquired video frames on a digital computing hardware. Yilmaz [25] conducted a survey of such object detection methods. Optical correlator (OC) [26,27] is another target detection method, performed by dedicated optical hardware. Therein, target recognition is realized by optical refraction, interference, and diffraction. OC has the advantages of inherent parallel processing due to optical Fourier Transform, and fast operation regardless of image size. Among its demerits are additional volume and mass due to electro-optical construction and additional power consumption for a laser diode. CV algorithms are superior by being easy to program and realized on a computer. They operate on chip size hardware which nowadays is very fast and can perform parallel computation, e.g., using a graphics processing unit (GPU). In this work we focus on CV to make the ODVS tracking sensor more versatile and easily implementable.

Capturing a target's position using a camera gives a 2D measurement, which is degenerated with respect to the 3D space. Therefore, the distance to the target is not directly observable. As a result, it is only possible to obtain a unit vector pointing at the target's relative position, which is equivalent to measuring the azimuth and elevation of the line-of-sight (LOS). For rendering the system observable, this work pursued a fusion of additional sensor, and a relative state estimation algorithm.

Relative motion measurements, which contain noise and various inaccuracies, are usually not accurate enough for target tracking. Therefore, filtering techniques are being used for relative state estimation. Many systems for target tracking are based on a Kalman Filter (KF). Kalman filtering utilizes a state prediction, based on a dynamical model, together with a measurement likelihood, based on an observation model. Those are conjugated with a series of measurements observed over time, to estimate the evolving state. In case the physics or sensors are described by nonlinear models, the Extended Kalman Filter (EKF) may be used. Other techniques, such as the stochastic algorithm presented in [28], can also be used.

For spacecraft formation flying, Segal et al. solved the non-cooperative satellite tracking problem, using a stereovision sensor, and an EKF [5]. Lichter used range images, and a KF [4]. There exist numerous additional applications such as people tracking [6], and vehicles tracking [29]. Nevertheless, an ODVS-based non-cooperative target tracking in space, has not been examined yet. Consequently, the main innovation of this paper is a thorough study of the integration and fine-tuning of various methods which enable the development of this important application.

With the main goal of having an autonomous spacecraft, navigating relatively to other space objects, the system is required to make autonomous decisions based on relative information. Contributing to that goal, the purpose of this paper is to present a method for utilizing ODVSs as relative navigation sensors. An emphasis is given on developing algorithms for navigating relatively to non-cooperative targets, achieving reliable relative information based on an ODVS as a tracking sensor.

This work presents models, simulations, and experimental results for spacecraft relative state estimation, using tracking by an onboard ODVS. The fundamental estimation algorithm is presented first. Then, the dynamical model, and the measurement model are described, followed by the computer vision detection algorithm. Finally, the simulation and experimental results are shown, and a space scalability analysis is described.

2. Methods

2.1. Relative state estimation

A space vehicle which is orbiting Earth and has an ODVS, will be referred to as the *camera* satellite. A different space object which is orbiting Earth at a nearby orbit, will be referred to as *target*.

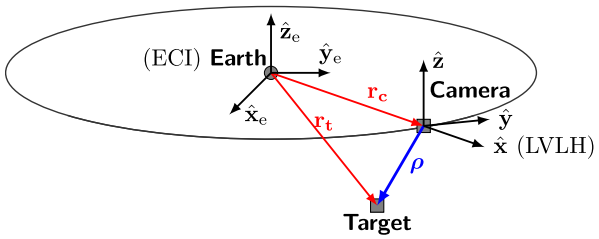

Fig. 1. Relative motion frame, originating at the camera satellite.

To formulate a state vector describing the relative state between the camera and the target, let us define the following reference frames: $\mathcal{E}$ is an Earth-Centered Inertial (ECI) reference frame, denoted by the unit vectors $\{\hat{\mathbf{x}}_e, \hat{\mathbf{y}}_e, \hat{\mathbf{z}}_e\}$; $\mathcal{L}$ is a Local-Vertical Local-Horizontal (LVLH) Euler–Hill reference frame fixed to the camera's center of mass (CM), with $\hat{\mathbf{x}}$ being a unit vector directed from the spacecraft radially outward, $\hat{\mathbf{z}}$ normal to the camera orbital plane, positive in the direction of the angular momentum vector, and $\hat{\mathbf{y}}$ completes the triad, see Fig. 1. In addition, for simplicity, we assume that the CM of the camera is coincident with $\mathcal{C}$, a Cartesian right-hand body-fixed reference frame attached to the ODVS's viewpoint (further elaborated in Section 2.3).

For relative navigation, information about the target's state, relative to the camera, is required. Focusing on relative translation solely, the vectors $\boldsymbol{\rho} = [x, y, z]^T \in \mathbb{R}^3$, and $\dot{\boldsymbol{\rho}} = [\dot{x}, \dot{y}, \dot{z}]^T \in \mathbb{R}^3$ denote respectively the position and velocity of the target's CM relative to the camera's CM, resolved in frame $\mathcal{L}$. The vector $\mathbf{x}$, which contains the relative position and velocity between the target and the camera, will be used as the state vector:

$$\mathbf{x} = \begin{bmatrix} \boldsymbol{\rho} \\ \dot{\boldsymbol{\rho}} \end{bmatrix} \in \mathbb{R}^6 \tag{1}$$

Obtaining such information using a monocular vision sensor is challenging, because the measurements are dimensionally sparse and noisy. Therefore, a filtering algorithm is required to estimate the relative state. The fact that the ODVS is a nonlinear sensor, as will be elaborated in Section 2.3, has led to choosing the EKF as the estimator. An explicit form of the EKF can be found in many textbooks, e.g. Ref. [1].

2.2. Dynamical model

The Clohessy-Wiltshire (CW) equations [30] can be used as a linearized dynamical model describing the relative motion between orbiting point-mass satellites, assumed to be rigid bodies:

$$\begin{cases} \ddot{x} - 2n\dot{y} - 3n^2 x = f_x \\ \ddot{y} + 2n\dot{x} = f_y \\ \ddot{z} + n^2 z = f_z \end{cases} \tag{2}$$

This system of linear differential equations, where $\{x, y, z\}$ are the components of the relative translation vector $\boldsymbol{\rho}$, describes the relative dynamics between closely-flying satellites, affected by differential perturbations, $\mathbf{u}(t) = [f_x, f_y, f_z]^T$, where n is the orbital angular velocity of the camera satellite, which is assumed to fly on a circular orbit, and is given by

$$n = \frac{2\pi}{T} = \sqrt{\frac{\mu}{a^3}} \tag{3}$$

where T is the orbital period, μ is Earth's gravitational parameter, and a is the semimajor axis of the camera orbit. CW equations are derived by linearization under the condition that the distance between the satellites is small relative to their orbital radius.

This dynamical model was used to formulate the state-space equations for the prediction phase in the EKF. The continuous equations can be written in linear form as

$$\dot{\mathbf{x}}(t) = \mathbf{F}\mathbf{x}(t) + \mathbf{G}\mathbf{u}(t) + \boldsymbol{\zeta}(t) \tag{4}$$

where $\mathbf{x}(t)$ is the state vector, $\mathbf{u}(t)$ represents the external forces, $\boldsymbol{\zeta}(t)$ is a white Gaussian process noise vector, and

$$\mathbf{F} = \begin{bmatrix} 0 & 0 & 0 & 1 & 0 & 0 \\ 0 & 0 & 0 & 0 & 1 & 0 \\ 0 & 0 & 0 & 0 & 0 & 1 \\ 3n^2 & 0 & 0 & 0 & 2n & 0 \\ 0 & 0 & 0 & -2n & 0 & 0 \\ 0 & 0 & -n^2 & 0 & 0 & 0 \end{bmatrix}, \quad \mathbf{G} = \begin{bmatrix} 0 & 0 & 0 \\ 0 & 0 & 0 \\ 0 & 0 & 0 \\ 1 & 0 & 0 \\ 0 & 1 & 0 \\ 0 & 0 & 1 \end{bmatrix} \tag{5}$$

The discrete transition matrix can be approximated by a Taylor-series expansion for $e^{\mathbf{F}\Delta t}$, and is calculated for relatively frequent sampling by

$$\boldsymbol{\Phi}_k \approx \mathbf{I} + \mathbf{F}\Delta t \tag{6}$$

which gives

$$\boldsymbol{\Phi}_k = \begin{bmatrix} 1 & 0 & 0 & \Delta t & 0 & 0 \\ 0 & 1 & 0 & 0 & \Delta t & 0 \\ 0 & 0 & 1 & 0 & 0 & \Delta t \\ 3n^2\Delta t & 0 & 0 & 1 & 2n\Delta t & 0 \\ 0 & 0 & 0 & -2n\Delta t & 1 & 0 \\ 0 & 0 & -n^2\Delta t & 0 & 0 & 1 \end{bmatrix} \tag{7}$$

where Δt is the sampling time, and $\mathbf{I}$ is the identity matrix. The discrete input matrix is calculated by

$$\boldsymbol{\Psi}_k = \int_0^{\Delta t} \boldsymbol{\Phi}(\tau)\mathbf{G}\, d\tau \tag{8}$$

which gives

$$\boldsymbol{\Psi} = \begin{bmatrix} \frac{\Delta t^2}{2} & 0 & 0 \\ 0 & \frac{\Delta t^2}{2} & 0 \\ 0 & 0 & \frac{\Delta t^2}{2} \\ \Delta t & n\Delta t^2 & 0 \\ -n\Delta t^2 & \Delta t & 0 \\ 0 & 0 & \Delta t \end{bmatrix} \tag{9}$$

The process noise covariance matrix is $\mathbf{Q} = E(\boldsymbol{\zeta}\boldsymbol{\zeta}^T)$. Assuming the process noise $\boldsymbol{\zeta}(t)$ represents acceleration uncertainty which is equal for all axes, and the noises of the different degrees-of-freedom (DOF) are assumed to be uncorrelated, the covariance matrix is given by

$$\mathbf{Q}(t) = \begin{bmatrix} 0 & 0 & 0 & 0 & 0 & 0 \\ 0 & 0 & 0 & 0 & 0 & 0 \\ 0 & 0 & 0 & 0 & 0 & 0 \\ 0 & 0 & 0 & \Phi_s & 0 & 0 \\ 0 & 0 & 0 & 0 & \Phi_s & 0 \\ 0 & 0 & 0 & 0 & 0 & \Phi_s \end{bmatrix} \tag{10}$$

where Φ_s is the power spectral density. The discrete process noise covariance matrix is calculated by

$$\mathbf{Q}_k = \int_0^{\Delta t} \boldsymbol{\Phi}(\tau)\mathbf{Q}\boldsymbol{\Phi}^T(\tau)\, d\tau \tag{11}$$

which gives

$$\mathbf{Q}_k = \Phi_s \begin{bmatrix} \frac{\Delta t^3}{3} & 0 & 0 & \frac{\Delta t^2}{2} & -2n\frac{\Delta t^3}{3} & 0 \\ 0 & \frac{\Delta t^3}{3} & 0 & 2n\frac{\Delta t^3}{3} & \frac{\Delta t^2}{2} & 0 \\ 0 & 0 & \frac{\Delta t^3}{3} & 0 & 0 & \frac{\Delta t^2}{2} \\ \frac{\Delta t^2}{2} & 2n\frac{\Delta t^3}{3} & 0 & \Delta t + 4n^2\frac{\Delta t^3}{3} & 0 & 0 \\ -2n\frac{\Delta t^3}{3} & \frac{\Delta t^2}{2} & 0 & 0 & \Delta t + 4n^2\frac{\Delta t^3}{3} & 0 \\ 0 & 0 & \frac{\Delta t^2}{2} & 0 & 0 & \Delta t \end{bmatrix} \tag{12}$$

After discretization, we write the prediction equations for the state and the estimation error covariance matrix:

$$\begin{cases} \mathbf{x}_k^- &= \boldsymbol{\Phi}_k \hat{\mathbf{x}}_{k-1} + \boldsymbol{\Psi}_k \mathbf{u}_{k-1} \\ \mathbf{P}_k^- &= \boldsymbol{\Phi}_k \hat{\mathbf{P}}_{k-1} \boldsymbol{\Phi}_k^T + \mathbf{Q}_k \end{cases} \tag{13}$$

where $\mathbf{x}_k^-$ denotes the predicted state vector at sample k, $\hat{\mathbf{x}}_{k-1}$ denotes the estimated state vector from the previous sample $k-1$, $\mathbf{u}_{k-1}$ denotes the external forces vector from the previous sample $k-1$, $\mathbf{P}_k^-$ is the predicted covariance matrix at sample k, $\hat{\mathbf{P}}_{k-1}$ is the estimated covariance matrix from the previous sample $k-1$, and $\mathbf{\Phi}_k, \mathbf{\Psi}_k, \mathbf{Q}_k$ are the discrete transition matrix, the discrete input matrix, and the discrete process noise covariance matrix at sample k as described above.

2.3. Measurement model

A measurement model is needed for both calibration of the ODVS and the estimation process. For the estimation, the measurement model is used for calculating the measurement likelihood and the Kalman gain. Image sensors capture discrete measurements every frame; hence, the nonlinear measurement equation is written using the discrete form

$$\mathbf{z}_k = \mathbf{h}(\mathbf{x}_k) + \boldsymbol{\nu}_k \tag{14}$$

where $\boldsymbol{\nu}_k$ is a white Gaussian noise vector. The discrete measurement-noise covariance matrix $\mathbf{R}_k$ consists of variances representing each measurement-noise source and is given by $\mathbf{R}_k = E(\boldsymbol{\nu}_k \boldsymbol{\nu}_k^T)$. The linearized measurement equations are related to the nonlinear equations through the Jacobian

$$\mathbf{H} = \left.\frac{\partial \mathbf{h}(\mathbf{x})}{\partial \mathbf{x}}\right|_{\mathbf{x}=\hat{\mathbf{x}}_k} \tag{15}$$

where $\hat{\mathbf{x}}_k$ is the estimated state vector at sample k. The discrete measurement likelihood equations take the following form:

$$\begin{cases} \mathbf{z}_k^- &= \mathbf{H}_k \mathbf{x}_k^- \\ \mathbf{S}_k &= \mathbf{H}_k \mathbf{P}_k^- \mathbf{H}_k^T + \mathbf{R}_k \end{cases} \tag{16}$$

where $\mathbf{z}_k^-$ denotes the measurement likelihood vector at sample k, $\mathbf{H}_k$ is the discrete measurement model matrix at sample k, and $\mathbf{S}_k$ is the measurement likelihood covariance matrix at sample k.

The Kalman gain of an EKF cannot be computed off-line, as possible with a KF, because $\mathbf{H}_k$ results from linearization of nonlinear functions, and it changes its values according to the current estimated state. Furthermore, the $\mathbf{H}_k$ matrix is required mainly for the calculations of the Kalman gain, whereas for the measurement likelihood, the nonlinear function $\mathbf{h}(\mathbf{x}_k)$ will give more accurate results [31].

2.3.1. Unified projection model

Axis convention is chosen as depicted in Fig. 2. Based on Mei [14], the projection of 3D points onto the 2D image plane can be described as follows:

1. World points in the mirror frame $\mathcal{C}$ are projected onto the unit sphere,
$$\{\boldsymbol{\rho}\}_{\mathcal{C}} \to \{\boldsymbol{\rho}_s\}_{\mathcal{C}} = \frac{\boldsymbol{\rho}}{\|\boldsymbol{\rho}\|} = \begin{bmatrix} x_s & y_s & z_s \end{bmatrix}^T \tag{17}$$
2. The points are transformed to a new reference frame $\mathcal{N}$, translated by $\mathbf{t}_n = \begin{bmatrix} 0 & 0 & \xi \end{bmatrix}^T$ where ξ is a mirror parameter which varies between 0, for a planar mirror and 1, for a parabolic mirror:
$$\{\boldsymbol{\rho}_s\}_{\mathcal{C}} \to \{\boldsymbol{\rho}_s\}_{\mathcal{N}} = \begin{bmatrix} x_s & y_s & z_s + \xi \end{bmatrix}^T \tag{18}$$
For a hyperbolic mirror $\xi = \frac{2c}{\sqrt{(2c)^2+(2p)^2}}$, where $2p$ is the semi-latus rectum and $2c$ is the distance between focal points. The relationship to the semimajor axis a, and the semiminor axis b is
$$\begin{cases} a &= \frac{\sqrt{(2c)^2+(2p)^2}-2p}{2} \\ b &= \sqrt{p(\sqrt{(2c)^2+(2p)^2}-2p)} \end{cases} \tag{19}$$
Considering the mirror parameter $\mathbf{v}_s = \{\xi\}$, both steps above could be unified as
$$\mathbf{s}(\mathbf{x}_k^-, \mathbf{v}_s) = \begin{bmatrix} \frac{x}{\|\boldsymbol{\rho}\|} & \frac{y}{\|\boldsymbol{\rho}\|} & \frac{z}{\|\boldsymbol{\rho}\|} + \xi \end{bmatrix}^T \tag{20}$$
3. The points are then projected onto the normalized image plane,
$$\mathbf{m}_u = \mathbf{n}(\boldsymbol{\rho}_s) = \begin{bmatrix} \frac{x_s}{z_s+\xi} & \frac{y_s}{z_s+\xi} & 1 \end{bmatrix}^T = \begin{bmatrix} x_u & y_u & 1 \end{bmatrix}^T \tag{21}$$
The vector-valued function $\mathbf{n}(\cdot)$ is bijective from $\{\boldsymbol{\rho}_s | z_s > -\xi\}$ to $\mathbb{R}^2$.
4. The undistorted points are projected onto the distorted normalized plane, modeling radial and tangential distortions using the $\mathbf{v}_d = \{k_1, k_2, p_1, p_2\}$ parameters. Imperfection of the lens shape is modeled by radial distortion, while an improper lens and camera assembly (e.g. misalignment) generates both radial and tangential distortions. Radial distortion can be modeled by
$$\begin{aligned} \mathbf{m}_u L(r_u) &= \mathbf{m}_u (k_1 r_u^2 + k_2 r_u^4) \\ r_u &= \sqrt{x_u^2 + y_u^2} \end{aligned} \tag{22}$$
Tangential distortion can be modeled by
$$d\mathbf{t} = \begin{bmatrix} 2p_1 x_u y_u + p_2(r_u^2 + 2x_u^2) \\ 2p_2 x_u y_u + p_1(r_u^2 + 2y_u^2) \end{bmatrix} \tag{23}$$
The total distortion is then written as
$$\mathbf{e}(\mathbf{m}_u, \mathbf{v}_d) = \mathbf{m}_u L(r_u) + d\mathbf{t} \tag{24}$$
where
$$\mathbf{e}(\mathbf{m}_u, \mathbf{v}_d) = \begin{bmatrix} x_u(k_1 r_u^2 + k_2 r_u^4) + 2p_1 x_u y_u + p_2(r_u^2 + 2x_u^2) \\ y_u(k_1 r_u^2 + k_2 r_u^4) + 2p_2 x_u y_u + p_1(r_u^2 + 2y_u^2) \end{bmatrix} \tag{25}$$
The distorted points can be written by adding the total distortion,
$$\mathbf{m}_d = \mathbf{d}(\mathbf{m}_u, \mathbf{v}_d) = \mathbf{m}_u + \mathbf{e}(\mathbf{m}_u, \mathbf{v}_d) \tag{26}$$
5. The final projection is given by
$$\mathbf{z} = \mathbf{k}(\mathbf{m}_d, \mathbf{v}_k) = \mathbf{K}_I \mathbf{m}_d \tag{27}$$
where $\mathbf{K}_I$ is the intrinsic camera parameter matrix, constructed from the focal length divided by the pixel size $\{\gamma_u = f/P_u, \gamma_v = f/P_v\}$, the skew coefficient $S = \gamma_v \tan\beta$ between $\hat{\mathbf{u}}$ and $\hat{\mathbf{v}}$, and the principal point, i.e. the translation from the optical center $[u_0, v_0]$:
$$\mathbf{K}_I = \begin{bmatrix} \gamma_u & S & u_0 \\ 0 & \gamma_v & v_0 \\ 0 & 0 & 1 \end{bmatrix} \tag{28}$$

Finally, the measurement model of Eq. (14) can be written as

$$\mathbf{z}_k = \mathbf{h}(\mathbf{x}_k^-, \mathbf{v}_t) \tag{29}$$

where $\mathbf{x}_k^-$ is the predicted state and

$$\mathbf{h} = \mathbf{k} \circ \mathbf{d} \circ \mathbf{n} \circ \mathbf{s}, \qquad \mathbf{v}_t = \{\mathbf{v}_s, \mathbf{v}_d, \mathbf{v}_k\} \tag{30}$$

The linearized measurement model $\mathbf{H}_{2\times 6}$ is calculated using the Jacobian

$$\mathbf{H}_k = \left.\frac{\partial \mathbf{h}(\mathbf{x}, \mathbf{v}_t)}{\partial \mathbf{x}}\right|_{\mathbf{x}=\mathbf{x}_k^-} = \underset{2\times 2}{\frac{\partial \mathbf{z}}{\partial \mathbf{m}_d}} \cdot \underset{2\times 2}{\frac{\partial \mathbf{m}_d}{\partial \mathbf{m}_u}} \cdot \underset{2\times 3}{\frac{\partial \mathbf{m}_u}{\partial \boldsymbol{\rho}_s}} \cdot \underset{3\times 6}{\frac{\partial \boldsymbol{\rho}_s}{\partial \mathbf{x}_k^-}} \tag{31}$$

The discrete measurement-noise covariance matrix $\mathbf{R}_k$ consists of variances representing each measurement-noise source. Assuming that the most significant noise is introduced by the non-observability of the depth, which could affect the different axes, depending on the target's location in space, the noise was assumed to be equal for both axes. The noises at $\hat{\mathbf{u}}$ and $\hat{\mathbf{v}}$ are assumed to be uncorrelated because the camera is calibrated and errors introduced by the computer vision algorithms are assumed to be uncorrelated. Thus,

$$\mathbf{R}_k = \begin{bmatrix} R_s & 0 \\ 0 & R_s \end{bmatrix} \text{ pixels}^2 \tag{32}$$

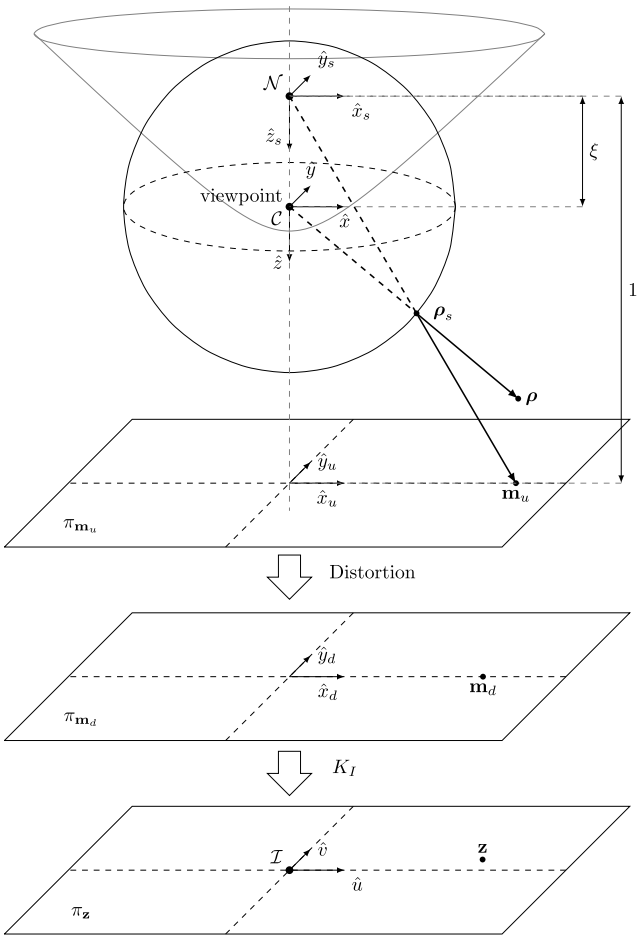

Fig. 2. Unified projection model.

2.3.2. Inverted unified projection model

In order to initialize the estimation process, an a-priori information about the initial state is required. It can be achieved by applying the inverted unified projection model on the first measurement.

For inverting the measurement model of Eq. (29), inversion of the intrinsic camera projection matrix is required,

$$\mathbf{m}_d = \mathbf{k}^{-1}(\mathbf{z},\, \mathbf{v}_k) = \mathbf{K}_I^{-1}\mathbf{z} \tag{33}$$

Because the distortion model of Eq. (26) is not analytically invertible, Mei [32] inverted the model using a recursive function,

$$\begin{cases} \mathbf{m}_u &= \mathbf{m}_d - \mathbf{e}^g \\ \mathbf{e}^g &= \mathbf{e}(\mathbf{m}_d - \mathbf{e}^{g-1}, \mathbf{v}_d) \\ \mathbf{e}^1 &= \mathbf{e}(\mathbf{m}_d, \mathbf{v}_d) \end{cases} \tag{34}$$

where g is the number of recursive iterations. Mei showed that $g = 4$ gives a reprojection error of less than a pixel. The recursive function converges towards the correct inverse if the distortion parameters $\mathbf{v}_d$ are strictly smaller than 1. Applying this method is computationally expensive; however, once obtained, the transformation of each image point can be pre-calculated and saved in a lookup table. Next, lifting is required, which is the inverse function $\mathbf{n}^{-1}(\cdot)$ of calculating point $\{\boldsymbol{\rho}_s\}_{\mathcal{N}}$ from a given point $\{\mathbf{m}_u\}_{\mathcal{N}}$:

$$\boldsymbol{\rho}_s = \mathbf{n}^{-1}(\mathbf{m}_u, \mathbf{v}_s) = \frac{\xi + \sqrt{1 + (1-\xi^2)(x_u^2 + y_u^2)}}{x_u^2 + y_u^2 + 1} \begin{bmatrix} x_u \\ y_u \\ 1 \end{bmatrix} + \begin{bmatrix} 0 \\ 0 \\ \xi \end{bmatrix} \tag{35}$$

As explained, the vector-valued function $\mathbf{n}(\cdot)$ is bijective for $z_s > -\xi$. Next, The points are transformed from frame $\mathcal{N}$ to $\mathcal{C}$,

$$\{\boldsymbol{\rho}_s\}_{\mathcal{N}} \rightarrow \{\boldsymbol{\rho}_s\}_{\mathcal{C}} = \begin{bmatrix} x_s & y_s & z_s - \xi \end{bmatrix}^T \tag{36}$$

To finalize, Eqs. (33)–(36) were used to obtain the inverted measurement model,

$$\frac{\boldsymbol{\rho}}{\|\boldsymbol{\rho}\|} = \mathbf{h}^{-1}(\mathbf{z}_k,\, \mathbf{v}_t) \tag{37}$$

2.3.3. Catadioptric camera calibration

In this work, Mei's catadioptric camera calibration toolbox [14] was used to calibrate the sensor before the experiments, while utilizing a chessboard pattern. ODVS parameters in the form of

$$\{\mathbf{v}_t\}_{1\times 10} = \begin{Bmatrix} \xi & k_1 & k_2 & p_1 & p_2 & S & \gamma_1 & \gamma_2 & u_0 & v_0 \end{Bmatrix}$$

were obtained. These parameters describe the specific catadioptric camera properties due to its mirror's conical shape, structure, assembly misalignment, camera-lens distortion and image sensor. They were used in the measurement model for creating artificial simulation measurements and throughout the experiments. Based on the unified projection model, the toolbox finds the intrinsic camera parameters when the user denotes the ODVS's mirror boundaries, and marks a straight line on the ODI. Next, an automatic process of grid marking is done for several images of a known chessboard pattern, placed at different positions. This is used for global minimization to find all the ODVS parameters, $\mathbf{v}_t$.

2.3.4. Ground station measurements

Since the depth realized from a vision sensor such as the ODVS is non-observable, a second data source is introduced, in order to check if sensor fusion improves the relative state estimation results.

Every time the camera and target pass above a ground station which measures their positions, the relative distance between them is used as another measurement (at a different sampling rate than the ODVS measurement). This can occur several times per orbit, depending on the orbit and the number of ground stations. Nevertheless, for evaluating the sensor fusion compared to using just the ODVS, we assume this occurs once every orbital period, and expand the measurement model of Eq. (14) to:

$$\mathbf{z}_k = \begin{bmatrix} \mathbf{z}_{1,k} & \mathbf{z}_{2,k} \end{bmatrix}^T \tag{38}$$

where $\mathbf{z}_{1,k}$, the ODVS measurement, is given by Eq. (29), and $\mathbf{z}_{2,k}$, the ground station measurement, is modeled as the Euclidean norm of the relative distance, $\boldsymbol{\rho}$:

$$\begin{cases} z_{2,k} = h_2(\mathbf{x}_k^-) \\ h_2(\mathbf{x}_k^-) = \left\| \boldsymbol{\rho}_k^- \right\| \end{cases} \tag{39}$$

When fusion occurs, the measurement-noise covariance matrix $\mathbf{R}_k$ is extended by the noise variance R_{s2} of the ground station measurement, assumed to be uncorrelated. Thus,

$$\mathbf{R}_k = \begin{bmatrix} R_{s1} & 0 & 0 \\ 0 & R_{s1} & 0 \\ 0 & 0 & R_{s2} \end{bmatrix} \tag{40}$$

where R_{s1} is in pixels^2, and R_{s2} is in km^2. In this work, the ground station measurement is assumed to be accurate, in order to check the sensor fusion effect on the non-observable distance between the objects, i.e. R_{s2} is small relative to R_{s1}.

2.4. Computer vision algorithms

As opposed to the simulation, wherein artificial measurements were created for the EKF, in a realistic scenario a detection method is required to obtain such measurements. In general, a detection method could be designed by different computer vision (CV) algorithms, while

(a) Noisy logical image mask produced from gray-scale thresholding.

(b) Mask edited by erosion followed by dilation using a small structural element.

(c) Mask edited by dilation followed by erosion using a large structural element and holes are filled.

(d) Robot is marked by a transparent red color, using the detection mask.

Fig. 3. Robot detection and marking using gray-scale thresholding and morphological operations.

different physical environments could require different solutions. As a consequence, a different algorithm should be designed for space operation and lab experiments.

In space, the observed scene usually has dark background with glare from the planet, the moon, and the sun. The image could include regions of the planet or the moon, but it will most likely avoid scenarios in which the sun will enter the FOV. In the lab, planar experiments included non-cooperative robots moving on a flat rectangular air-table, as described in Section 3.2. To emulate the space environment and render the experiment detections more realistic, the background outside the table was detected and masked. This was done in order to remove noise and make the observed scene clear from objects, as expected in space. Next, targets realized by robots, were detected from the ODI frames, overcoming different illumination conditions and reflections, which cause noisy images. This was done by developing the CV algorithms that were used throughout the experiments. These algorithms can be manipulated or changed to account for the conditions in space missions.

2.4.1. Target detection

Considering an object in the space environment, the following assumptions are used. The object has an unknown size and shape, some illumination is assumed to exist, and this illumination emphasizes foreground targets on top of a dark background. For object tracking in this research and for estimating the relative state, the target is represented by the object's center of area. Hence, target representation is given by a single point, located at the center of the detected image area, assuming it represents the physical center of mass (CM). The CM location is assumed to have a normally distributed noise, with zero mean and error boundaries determined by the detected shape's contour. A gray-scale thresholding was chosen to detect the bright robots on top the dark table, followed by morphological filtering. This solution enabled the detection of target properties such as CM and shape.

For simplification, we assume a single target. Hence, a general large shape can be searched for and marked as a target, by masking all surrounding pixels. A gray-scale threshold was calibrated for the conditions of the experiments (illumination, object colors, etc.). All pixels possessing a value above that threshold were marked as true. Thus, a noisy logical black and white mask was obtained, containing different connected areas, as seen in Fig. 3(a) (for extended methods, refer to [33]). Then, morphological operations were performed in order to connect robot regions with bad detection and create solid convex regions while removing the noise. As shown in Fig. 3(b), in order to erase small regions, which most likely represent noise or non-accurately detected regions, a small disk-shaped structural element was used, positioning its center on a peripheral pixel of each of the connected regions, marked as true, and moving that element along the circumference of those regions while eroding the shape. This was followed by a similar operation of dilation using the same disk size structural element to preserve the detection area. At the next step, Fig. 3(c), a dilation was performed, followed by an erosion using a larger disk-shaped structural element, to connect separated regions and make the regions rounder. Then, the remaining holes were filled to remove noise from the detected regions themselves.

For the final object detection, connected regions of a certain calibrated size (number of pixels) were searched for, and the following information was collected: center of region; bounding box of the region; major axis and minor axis of the correlated ellipse, possessing the same second area moments as those of the detected region; orientation of the major axis relative to the $\hat{\mathbf{u}}$ axis, which is the horizontal axis of the image plane's reference frame $\mathcal{I}$. In order to display the detected robots, a segmentation of their region in the frame was done by marking it with a transparent red color, Fig. 3(d).

3. Results

3.1. Simulations

Simulating the filtering algorithm enabled comparing the usage of simulated ODVS measurements versus ground station measurements and a fusion thereof. Fig. 4 describes the general structure of the simulation.

The reference data is defined by assuming an ODVS is orbiting at Low-Earth Orbit (LEO), at an altitude of $h_C = 550$ km, and a target object is orbiting earth in a nearby orbit. The target's relative position can be described by the solution to the CW equations (2):

$$\begin{cases} x(t) = (-3x_0 - \frac{2}{n}\dot{y}_0)\cos nt + \frac{\dot{x}_0}{n}\sin nt + 4x_0 + \frac{2}{n}\dot{y}_0 \\ y(t) = \frac{2}{n}\dot{x}_0\cos nt + (6x_0 + 4\frac{\dot{y}_0}{n})\sin nt + y_0 - \frac{2\dot{x}_0}{n} - 3t(2nx_0 + \dot{y}_0) \\ z(t) = z_0\cos nt + \frac{\dot{z}_0}{n}\sin nt \end{cases} \tag{41}$$

together with the following initial conditions:

$$\begin{aligned} x_0 &= 0.1\ \text{km} & \dot{x}_0 &= 0\ \frac{\text{km}}{\text{s}} \\ y_0 &= 0\ \text{km} & \dot{y}_0 &= -2nx_0\ \frac{\text{km}}{\text{s}} \\ z_0 &= 0\ \text{km} & \dot{z}_0 &= 0\ \frac{\text{km}}{\text{s}} \end{aligned} \tag{42}$$

The constraint $\dot{y}_0 = -2nx_0$ creates a periodic relative orbit by eliminating the drift from the solution. The orbit's angular velocity can be calculated from Eq. (3) while the semimajor axis a equals the sum of Earth's radius R_E, and the camera's height h_C. Propagating Eq. (41) gives the relative orbit, which is shown in Fig. 5. The target is tracked by the ODVS, and then projected onto the camera's image plane as the main measurement $\mathbf{z}_{1,k}$, using the measurement model of Eq. (29). To emulate a real ODVS, the model calibration parameters (of Section 2.3.3) were taken from the lab system. To create realistic detections, white noise was added to the ODI projection. In accordance

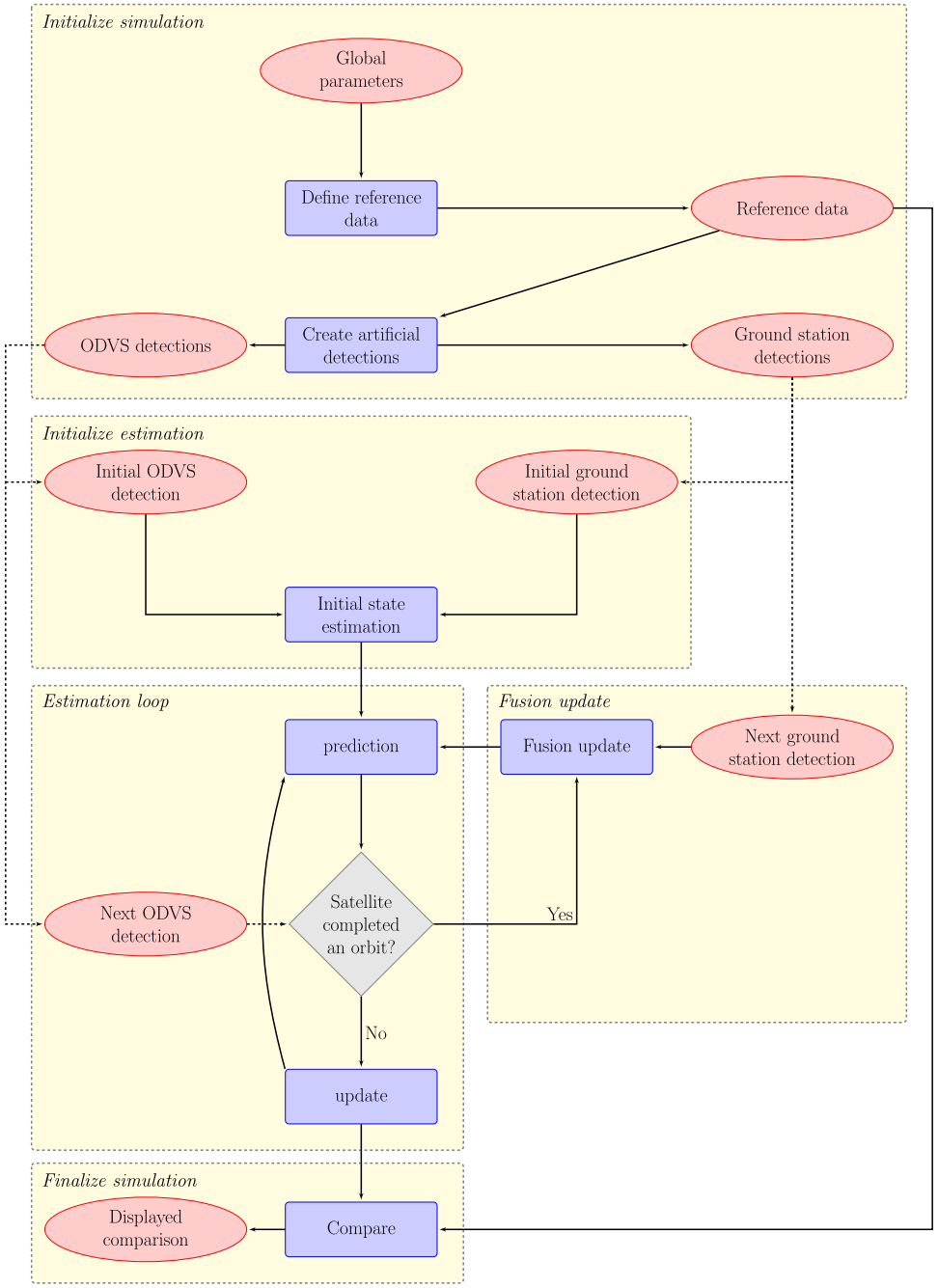

Fig. 4. Simulation structure.

with the experiments of the following section and a space scalability analysis, an average number of 90 pixels which represent a target at the image plane, was used as 3σ of the measurement noise normal probability distribution. Simulated detections are presented in Fig. 6.

Ground station measurements of relative position $\mathbf{z}_{2,k}$ were artificially created from the reference data. To that end, we assume that a pass above a ground station occurs once every orbital period. The orbital period is

$$T = \frac{2\pi}{n} = 5739 \text{ s} \tag{43}$$

The simulation was executed for $6.2T$, and enabled 6 measurement updates.

A comparison was made between relative state estimation using only ODVS, only ground station measurements and fusion thereof. The results are shown in Figs. 7, 8. The estimation errors are presented on a logarithmic scale, and the time is given in orbital periods. The errors in all 6 components of the relative state are represented in the Cartesian coordinate system $\mathcal{C}$.

Using only ground station measurements yields large estimation errors. For the x and y components of the relative position error, using only ODVS measurements gives results with an error of up to 70 m, while using fusion of both measurements gives results with an error as small as 0.3 m. Considering the absolute reference values range between 0–200 m, the sensors fusion gives the best relative position estimation with an error of approximately 1% with respect to the reference. For the z and $\dot{z}$ components of the relative error, using only ODVS seems as good as using fusion. This is assumed to be because the non-observable depth affected less the z axis, as the relative motion was within the xy plane. To summarize, it is observed that the best results

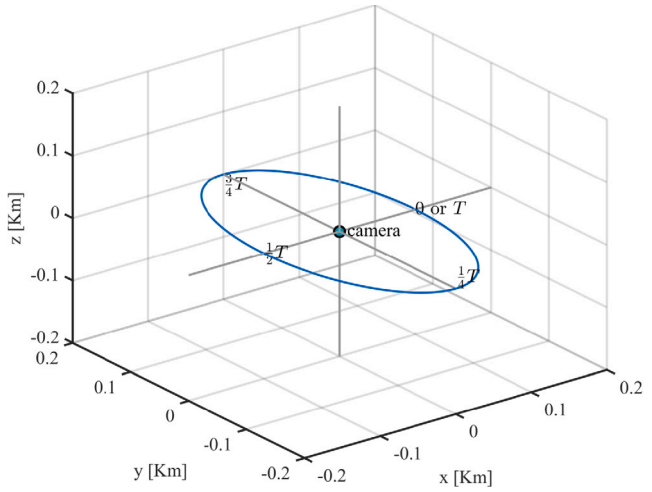

Fig. 5. Reference data given as the relative orbit of the target object with respect to the camera satellite, given at the camera's body-fixed coordinate system, $\mathcal{C}$.

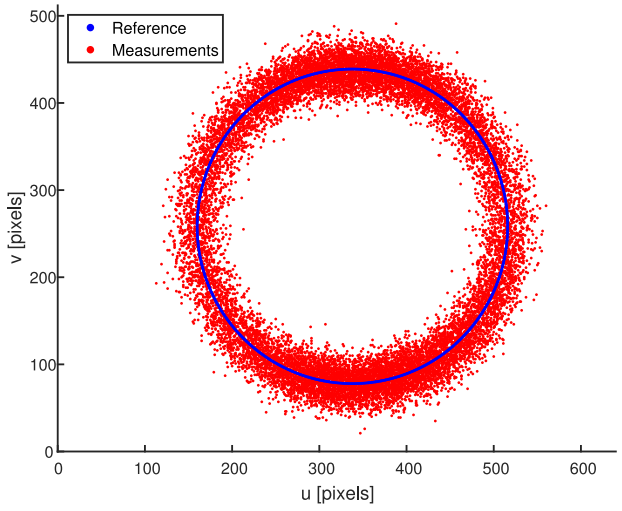

Fig. 6. All Target detections, projected to the omnidirectional image.

and highest accuracy were achieved when the estimation utilized fusion of ODVS measurements with ground station measurements. Estimating the relative state using ODVS only is a good option, if the depth can be bounded by calibration of the filter or by other means.

3.2. Experiments

Planar experiments conducted in the Distributed Space Systems Lab (DSSL) at Technion, included estimating the state of non-cooperative robots, relative to a robot equipped with an ODVS, observing 360° horizontally, without additional sensors. The lab setup is shown in Fig. 9(a). It includes robots moving on a frictionless air-bearing table. The circumference of the table was marked by a red tape in order to delineate the table as the zone for the CV detection algorithm.

Reference data of the actual position of each robot was recorded using an overhead camera with a fisheye lens, observing the complete surface of the air-table. For reference, the robots were detected using different CV algorithms, designed to identify the different robots. In addition, the detections by the fisheye camera were used for controlling the robot motion in closed loop. The structure of the ODVS used in the lab is shown in Fig. 9(b).

Two scenarios are shown in Fig. 10: The target is moving in a linear motion on a straight line; and in a circular motion orbiting the camera. The results are the estimated 6 dimensional relative state vector $\mathbf{x}$ represented in the camera frame $\mathcal{C}$. Note that having a state vector represented by a Cartesian coordinate system incorporates the depth projection into each axis. But, as mentioned before, the depth is not observable. Therefore, some of the comparisons were made using a spherical coordinate system, attached to the camera's CM, referred to as $\mathcal{S}$, to isolate the depth into a single axis. The spherical axes of $\mathcal{S}$ are range $\hat{\boldsymbol{\rho}}$, azimuth $\hat{\boldsymbol{\theta}}$, and elevation $\hat{\boldsymbol{\phi}}$. The transformation from the Cartesian frame $\mathcal{C}$ to the spherical frame $\mathcal{S}$ is given by

$$\begin{cases} \rho_k &= \sqrt{x_k^2 + y_k^2 + z_k^2} \\ \theta_k &= \arctan\left(\frac{y_k}{x_k}\right) \\ \phi_k &= \arctan\left(\frac{z_k}{\sqrt{x_k^2+y_k^2}}\right) \end{cases} \tag{44}$$

The covariance matrix represented in Cartesian frame ${}^{c}\mathbf{P}$ is rotated to the spherical frame ${}^{s}\mathbf{P}$ according to

$${}^{s}\mathbf{P}_k = \mathbf{R}_{s,k}\, {}^{c}\mathbf{P}_k\, \mathbf{R}_{s,k}^T \tag{45}$$

The rotation matrix $\mathbf{R}_s$ is given by

$$\mathbf{R}_{s,k} = \begin{bmatrix} \cos\phi_k \cos\theta_k & \cos\phi_k \sin\theta_k & \sin\phi_k \\ -\sin\theta_k & \cos\theta_k & 0 \\ -\sin\phi_k \cos\theta_k & -\sin\phi_k \sin\theta_k & \cos\phi_k \end{bmatrix} \tag{46}$$

where at each time step t_k, the azimuth and elevation are calculated according to Eq. (44).

3.2.1. Linear motion

Fig. 10(a) shows the experimental setup, in which the target robot is moving on a straight line and the ODVS is mounted on the robot in the center. The target robot moved from one corner of the table to the adjacent corner.

State prediction is given by Eq. (13). In this experiment, we assumed no external forces, hence $\mathbf{u} = \mathbf{0}$. A constant linear velocity motion model was used for the fundamental matrix,

$$\boldsymbol{\Phi}_k = \begin{bmatrix} 1 & 0 & 0 & \Delta t & 0 & 0 \\ 0 & 1 & 0 & 0 & \Delta t & 0 \\ 0 & 0 & 1 & 0 & 0 & \Delta t \\ 0 & 0 & 0 & 1 & 0 & 0 \\ 0 & 0 & 0 & 0 & 1 & 0 \\ 0 & 0 & 0 & 0 & 0 & 1 \end{bmatrix} \tag{47}$$

where $\Delta t = 0.0939$ s is the camera sampling rate. The process noise $\boldsymbol{\zeta}$ is assumed to reflect only uncertainties in the accelerations of the robot, which are equal for all axes. The noises of the different dimensions are assumed to be uncorrelated. This yields the same process noise covariance matrix as in Eq. (10) which is discretized according to Eq. (11) to obtain

$$\mathbf{Q}_k = \boldsymbol{\Phi}_s \begin{bmatrix} \frac{\Delta t^3}{3} & 0 & 0 & \frac{\Delta t^2}{2} & 0 & 0 \\ 0 & \frac{\Delta t^3}{3} & 0 & 0 & \frac{\Delta t^2}{2} & 0 \\ 0 & 0 & \frac{\Delta t^3}{3} & 0 & 0 & \frac{\Delta t^2}{2} \\ \frac{\Delta t^2}{2} & 0 & 0 & \Delta t & 0 & 0 \\ 0 & \frac{\Delta t^2}{2} & 0 & 0 & \Delta t & 0 \\ 0 & 0 & \frac{\Delta t^2}{2} & 0 & 0 & \Delta t \end{bmatrix} \tag{48}$$

while $\boldsymbol{\Phi}_s$ enables calibration of the filter.

Measurement likelihood is given by Eq. (16). For the measurement model, the nonlinear unified projection model of Eq. (29) was used together with the calibrated parameters of the ODVS. For calculating the covariance matrix $\mathbf{S}_k$, the linearized measurement model $\mathbf{H}_k$ was used, Eq. (31). The discrete measurement-noise covariance matrix $\mathbf{R}_k$ is given by Eq. (32).

Fig. 11 depicts the estimated relative state error represented in the coordinate system $\mathcal{C}$. As observed, errors in the position states are up

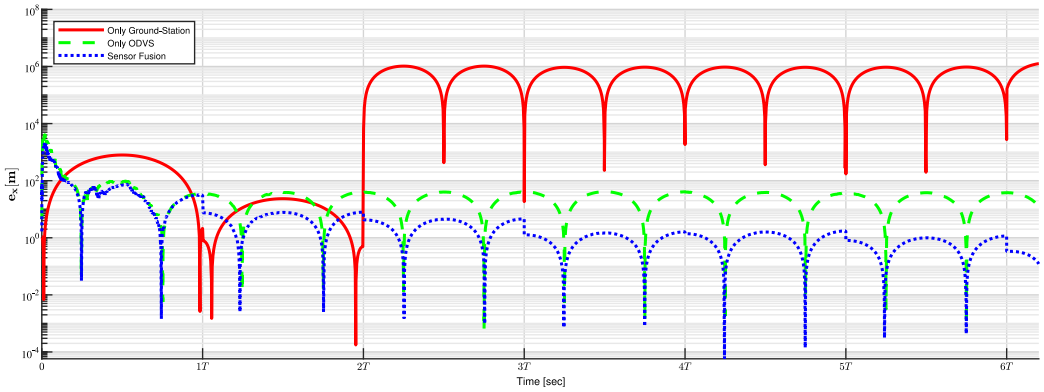

(a) x estimation error comparison.

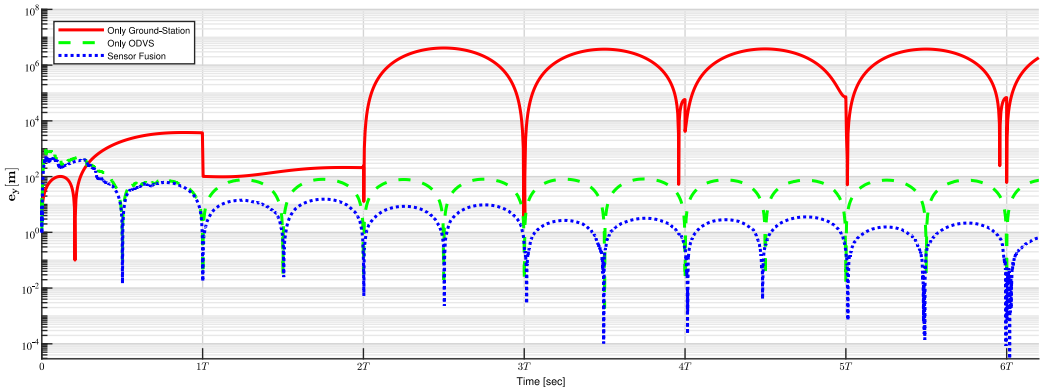

(b) y estimation error comparison.

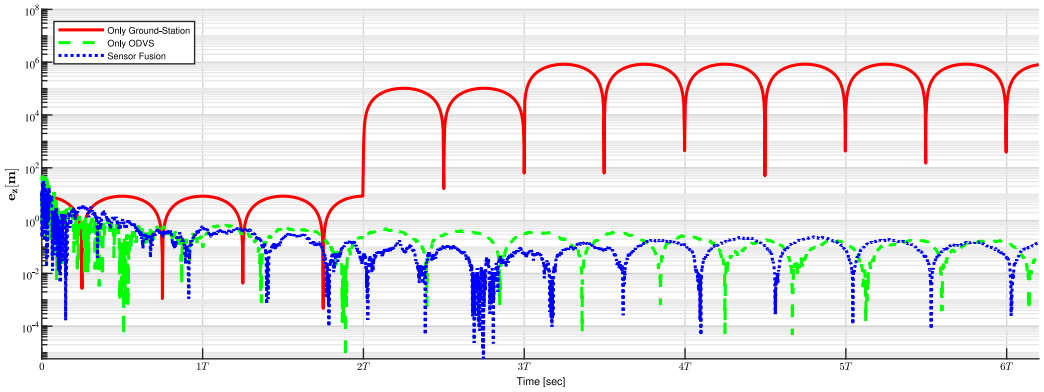

(c) z estimation error comparison.

Fig. 7. Comparison between different measurements and their effect on the Cartesian relative position error components.

to 0.3 m, errors in the velocity states are up to 0.1 m, and all errors are bounded by the standard deviation (STD). Looking at the shape of the STD of the $\hat{\mathbf{x}}$ and $\hat{\mathbf{y}}$ axes, the variance of the $\hat{\mathbf{x}}$ axis is maximal while the target is crossing the $\hat{\mathbf{x}}$ axis, and the variance of the $\hat{\mathbf{y}}$ axis is larger while the robot is shifting farther on the $\hat{\mathbf{y}}$ direction. Having a target crossing the scene horizontally is expected to cause larger variance, as an effect of the non-observable depth, alternating between the $\hat{\mathbf{x}}$ and $\hat{\mathbf{y}}$ axes, according to the target's azimuth relatively to the camera. STD values of the relative velocity states converge towards zero, indicating that using the constant velocity motion model was reasonable. A small error is observed in the $\hat{\mathbf{z}}$ direction because the motion was only in the xy plane.

Fig. 12 presents the estimated relative position states together with the reference, all represented in the spherical coordinate system $\mathcal{S}$. A good tracking is observed for all states but a particularly accurate result is observed for the azimuth. Considering the planar motion of the robots, the apparent elevation change requires a clarification. It results from a constant height difference between the camera and the target. This height difference causes a change in the vertical viewing angle as a function of the varying range to the target. Furthermore, that is the reason for the inverted behavior of the elevation and range axes. It can be seen in the middle of the target's motion, where the range is the smallest and the elevation is the highest.

3.2.2. Circular motion

Fig. 10(b) presents the experiment setup, in which the target robot is moving on a circular orbit and the ODVS is mounted on the robot in the center.

Here we used a constant angular velocity motion model which utilizes the fundamental matrix of constant linear velocity motion,

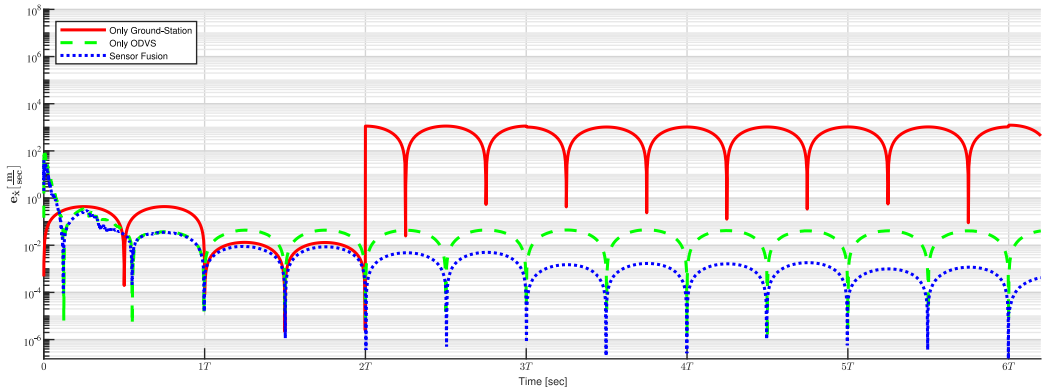

(a) $\dot{x}$ estimation error comparison.

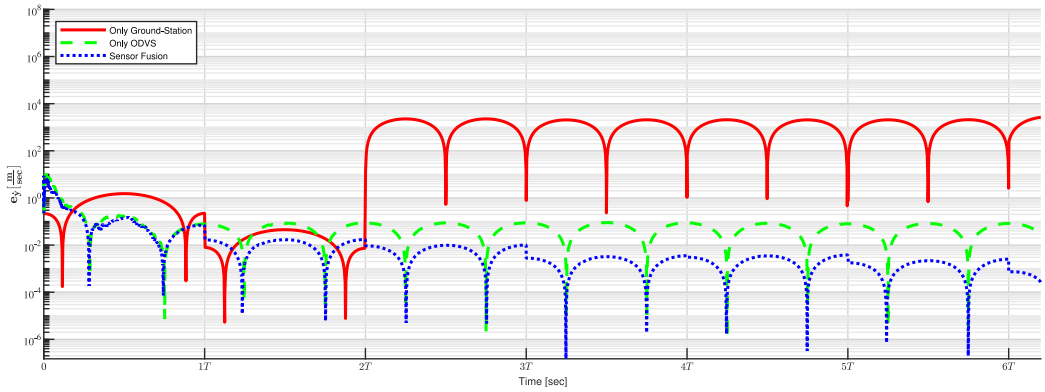

(b) $\dot{y}$ estimation error comparison.

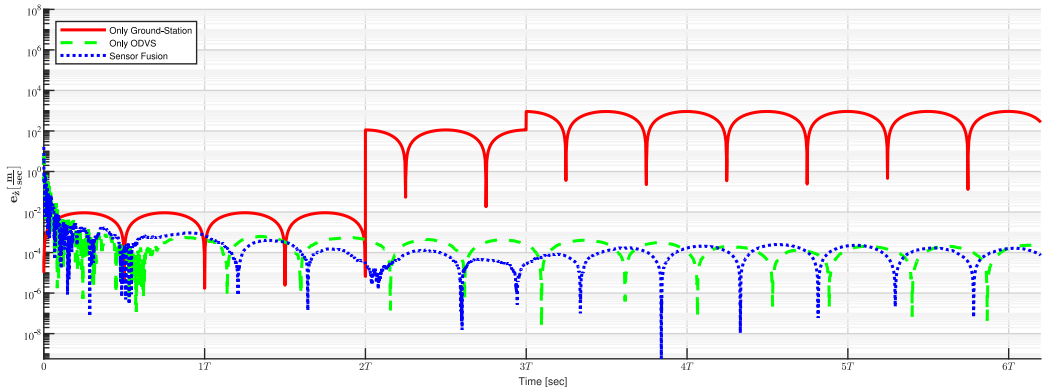

(c) $\dot{z}$ estimation error comparison.

Fig. 8. Comparison between different measurements and their effect on the Cartesian relative velocity error components.

Eq. (47), with $\Delta t = 0.0939$ s as before. In this scenario, the centripetal acceleration is modeled as an external force; hence $\mathbf{u} = \boldsymbol{\omega} \times (\boldsymbol{\omega} \times \boldsymbol{\rho})$ and the input matrix is given by:

$$\boldsymbol{\Psi}_k = \begin{bmatrix} \frac{\Delta t^2}{2} & 0 & 0 \\ 0 & \frac{\Delta t^2}{2} & 0 \\ 0 & 0 & \frac{\Delta t^2}{2} \\ \Delta t & 0 & 0 \\ 0 & \Delta t & 0 \\ 0 & 0 & \Delta t \end{bmatrix} \tag{49}$$

The process noise is assumed to be as in the former scenario. Hence, the process noise covariance matrix of Eq. (48) was used. The measurement model is the nonlinear unified projection model of Eq. (29), the same as in the former scenario.

Fig. 13 presents the estimated relative states together with its reference, represented in the spherical coordinate system S. The results contain the range, azimuth and their rate of change, because the motion is evolving in the horizontal plane. As expected, the estimated range ρ drifts while the estimated azimuth θ, follows the reference accurately. The estimated velocity graphs present similar results. The errors in range cannot be compensated by the ODVS measurements. As those are not informative in that direction. $\dot{\theta}$ starts from zero and rises to an approximately constant value. This is in accordance with the target's motion, which starts from rest and accelerates to orbit the camera at an approximately constant angular velocity. The chosen motion model adds to the presented errors because it is formed by a linearization of a nonlinear motion. The centripetal acceleration linearly manipulates each discrete step of the circular path, by rotating the direction of motion. The accumulative error is expressed in the ρ and $\dot{\rho}$.

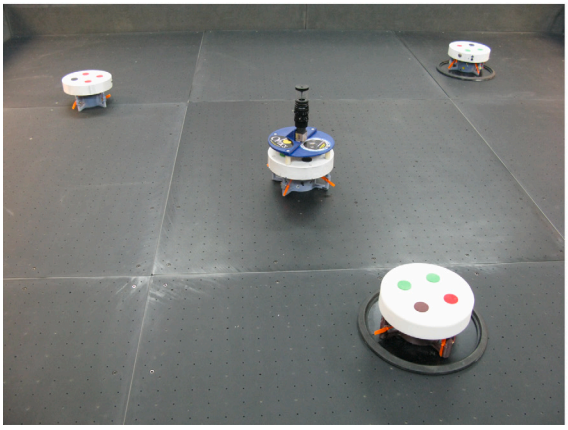

(a) Lab setup constructed of several robots placed on a frictionless air-bearing table. *Camera* robot has the ODVS mounted upon it. The other robots are referred to as *targets*.

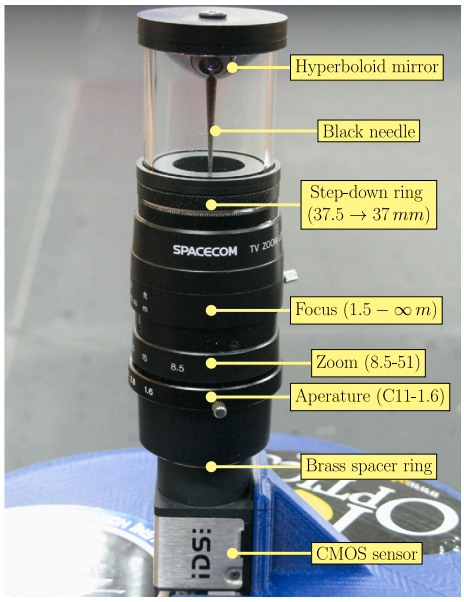

(b) The structure of the ODVS used in the lab.

Fig. 9. Lab setup.

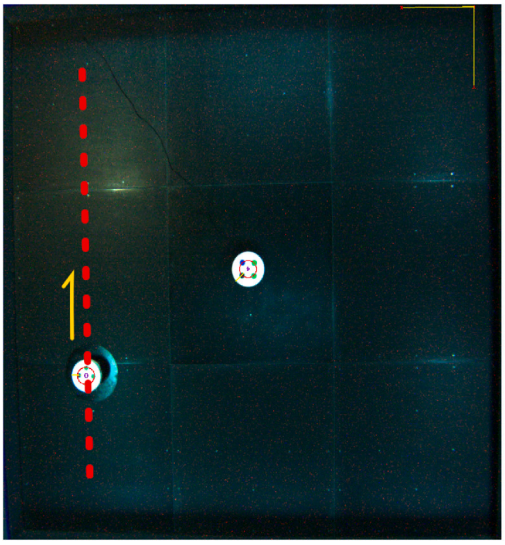

(a) Top view from the overhead camera. The ODVS is mounted on the robot in the center (*camera*). The *target* robot is moving in a straight line, which is marked by red path while a yellow arrow denotes the direction of motion.

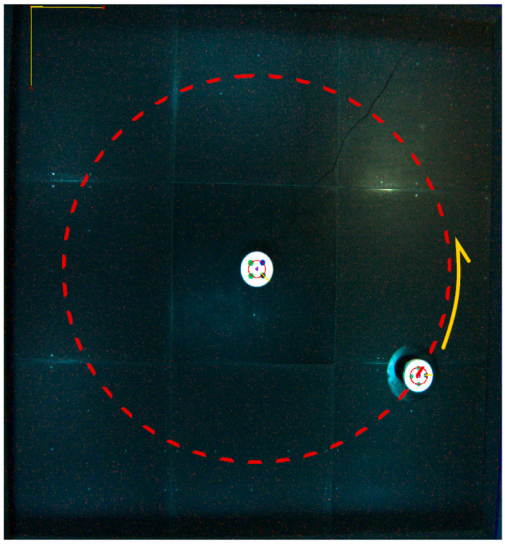

(b) Top view from the overhead camera. The ODVS is mounted on the robot in the center (*camera*). The *target* robot is moving in a circular motion, which is marked by red path while a yellow arrow denotes the direction of motion.

Fig. 10. Two experimental scenarios.

Fig. 14 presents the estimated relative position error of the target, represented by the spherical coordinate system, $\mathcal{S}$. These graphs are presented to give another perspective on the non-observability of the range. They show that the azimuth error is bounded by the STD for more than 66% of the time, while the range error is not.

Fig. 15 presents the estimated relative state for calibrated EKF together with its reference, represented in the spherical coordinate system $\mathcal{S}$. Optimal tuning of the EKF was performed under the consistency test condition [34]. These graphs present the results of the same experiment but using different values for the calibration of the EKF. As can be seen, when the estimator is optimally calibrated, and there is a better balance between the errors of the motion model and the errors of the measurement model, it is possible to bound the non-observable depth.

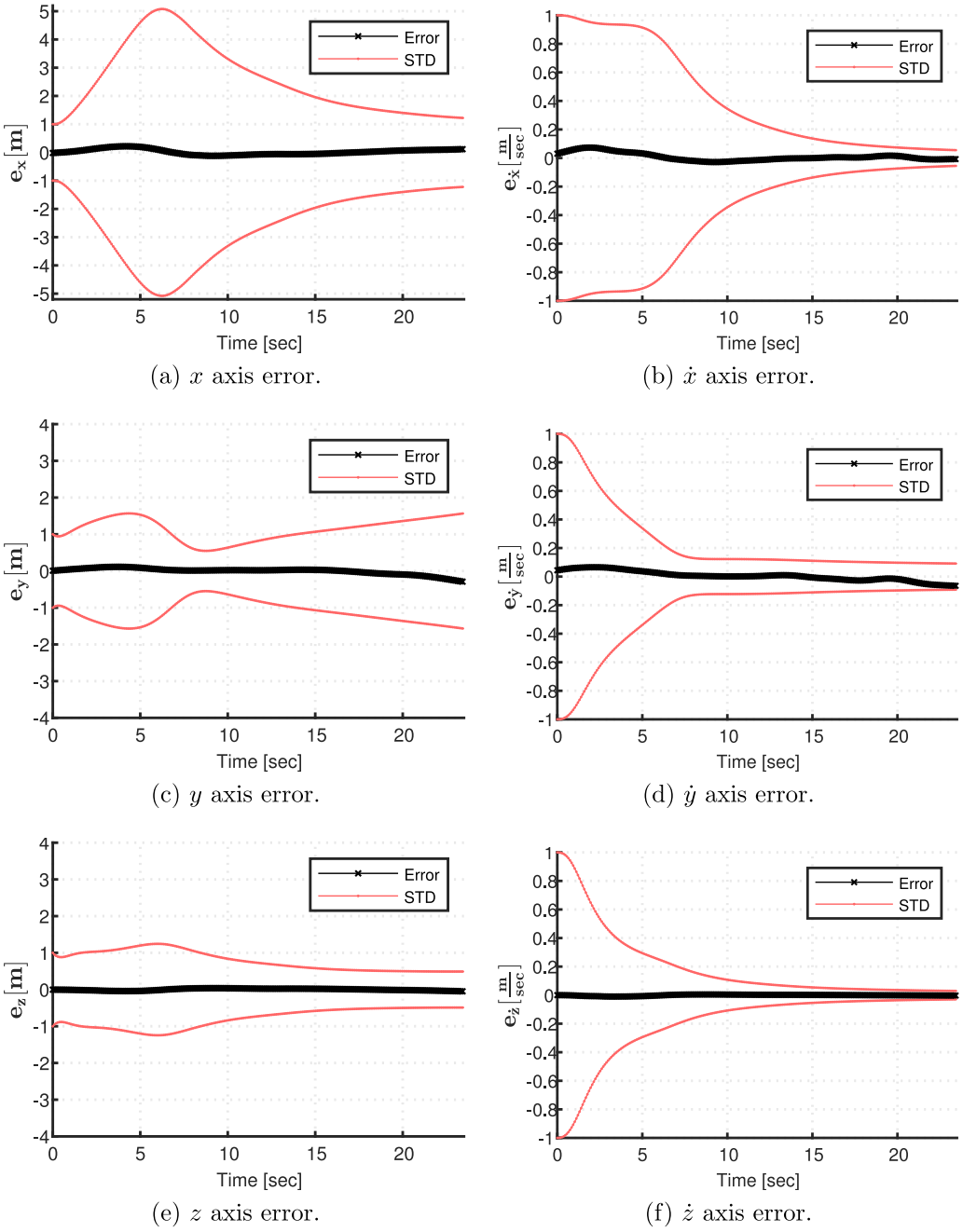

(a) x axis error. (b) $\dot{x}$ axis error.

(c) y axis error. (d) $\dot{y}$ axis error.

(e) z axis error. (f) $\dot{z}$ axis error.

Fig. 11. Relative state estimation error, for the case of linear motion, represented in the Cartesian coordinate system, $\mathcal{C}$.

4. Space scalability analysis

The results of the simulation and lab experiments give an indication of the suitability of the algorithms and hardware for implementation in space. However, to that end, a scalability analysis is required. The analysis defines a potentially real world scenario of an ODVS mounted on a satellite, tracking a target at an adjacent orbit, within its FOV. The ODVS in space should have compatible performance to its laboratory prototype and more specifically, compatible resolution. System parameters are shown to fit the desired target size and range in the example, and can be adjusted according to the scenario.

A full-frame format is a digital image sensor format that is the same size as a 35 mm film format (24 mm × 36 mm). The image sensor format of a digital camera determines the angle of view of a particular lens when it is being used with that particular sensor. The format size ratio (relative to the full-frame format) is known as the FOV crop-factor or just Crop Factor (CF).

For a given number of pixels, the larger sensor allows for larger pixels or photosites, that provide wider dynamic range and lower noise at high ISO levels. As a consequence, full-frame format may produce better quality images in certain high contrast or low light situations.

When designing an ODVS, the desired sensor should fit telephoto photography (smaller sensor), while the wide angle photography is achieved by the shaped mirror (hyperboloid in our case). On the other hand, having the ODVS operating in space, is likely to cause high contrast and low light in sun-hidden locations in the orbit. Hence, both larger and smaller sensors could benefit the system at different scenarios.

ODVS resolution, as a function of target size and distance, was investigated. Calculations are explained below, parameters are visualized

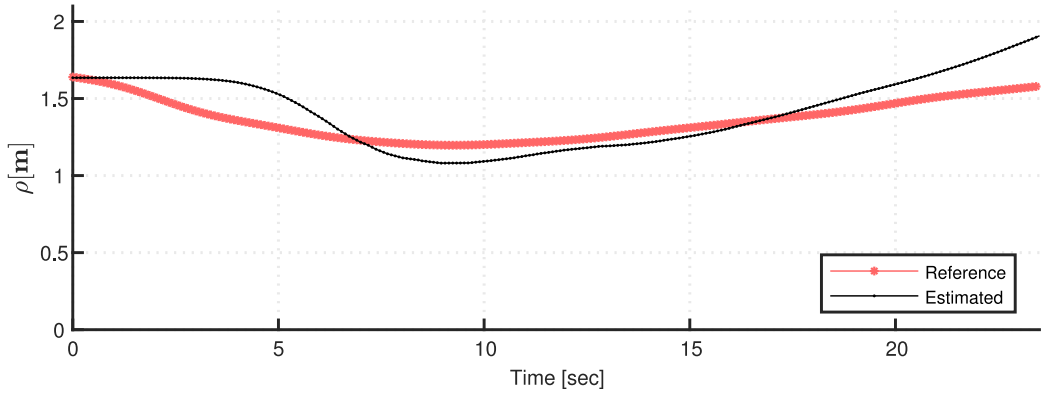

(a) State of ρ axis.

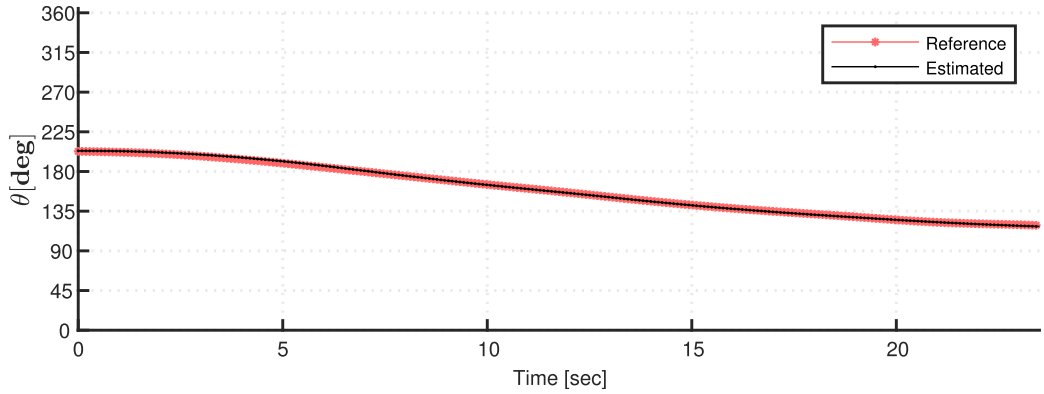

(b) State of θ axis.

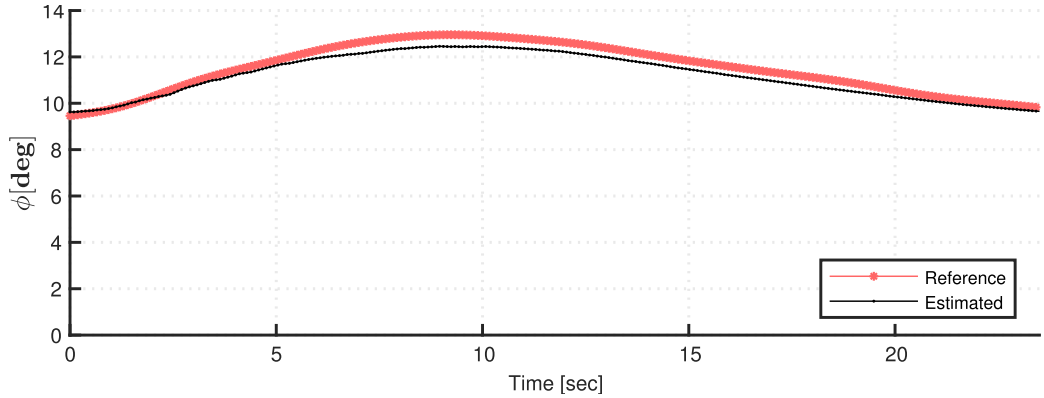

(c) State of ϕ axis.

Fig. 12. Estimated relative states, for the case of linear motion, represented in the spherical coordinate system, $\mathcal{S}$.

in Fig. 16, and numerical results are presented in Tables 1 and 2. The following discussion answers two key questions:

First, using the same system parameters as in the laboratory but for a different target distance, what will be the target size for which equivalent resolution performance will be obtained? Second, for desired target distance and size, how should the system parameters be changed, in order to get equivalent resolution?

4.1. First scenario

At a range of 100 m, the corresponding target size can be calculated from the ODVS parameters of the laboratory experiment. There, the infinitesimal target area which corresponds to 1 pixel of the image sensor, dT, is given by dividing the apparent target area, T_s, by the number of pixels representing the target in the image sensor, T_p:

$$dT = \frac{T_s}{T_p} \tag{50}$$

The corresponding infinitesimal solid angle[1] $d\nu$ is given by dividing the infinitesimal target size by the squared distance from the viewpoint to the target, d:

$$d\nu = \frac{dT}{d^2} \tag{51}$$

[1] In geometry, a solid angle is a measure of the amount of the FOV, from some particular point, that a given object covers. In the International System of Units (SI), a solid angle is expressed in a dimensionless unit called a steradian (sr).

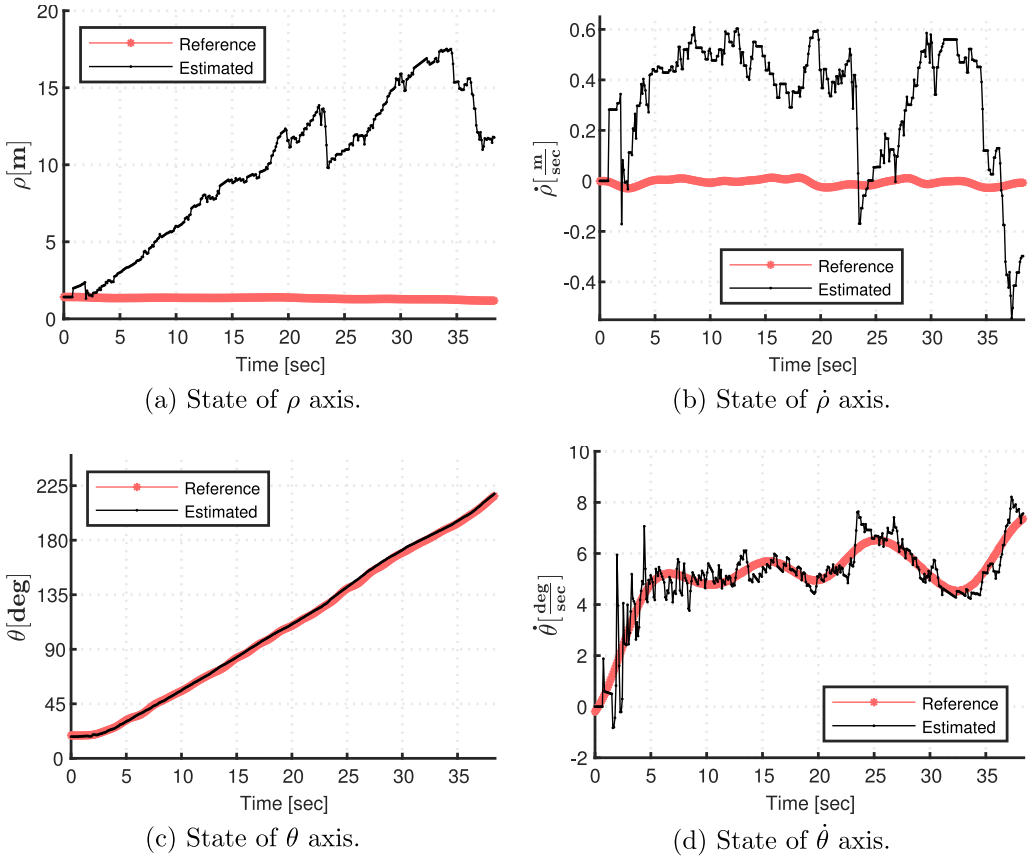

(a) State of ρ axis. (b) State of $\dot{\rho}$ axis.

(c) State of θ axis. (d) State of $\dot{\theta}$ axis.

Fig. 13. Estimated relative state, for the case of circular motion, represented by the spherical coordinate system, S.

In this first examined scenario, an ODVS with the same parameters as in the lab is considered. Thus, the space system has an infinitesimal solid angle of $3.681 \cdot 10^{-5}$ sr as the lab system has. Furthermore, the target is considered to be represented by the same number of pixels in both systems. The only difference is that the observed target is located at a different distance of $d_{space} = 100$ m. Substituting Eq. (50) in (51) and considering both systems has the same parameters, yields the following relation:

$$\frac{T_{space}}{T_s} = \left(\frac{d_{space}}{d}\right)^2 \tag{52}$$

Here, the ratio between the target sizes equals the squared ratio between the distances.

As can be seen in Table 1, in order to obtain equivalent performance in space, for a target 100 m away from the camera, the apparent target area should be at least 33.131 m^2. For smaller targets, we refer to the second scenario.

4.2. Second scenario

For space target sizes on the order of 1 m^2 and a range of 150 m, the ODVS parameters are presented in Table 2. In order to detect the target equivalently to the lab experiment, the target should be projected to 90 pixels in the image sensor. According to Eq. (50), this means that 1 pixel should represent an infinitesimal target area of 0.0111 m^2 and the corresponding solid angle, given by Eq. (51), will be $4.938 \cdot 10^{-7}$ sr. The ODVS resolution can be described by the relation between 1 image sensor pixel, to the infinitesimal solid angle to the target, $\frac{1}{dv}\,[\frac{1}{\text{sr}}]$. Thus, the desired ODVS resolution is $2.025 \cdot 10^6\ \frac{1}{\text{sr}}$. Comparing the ODVS resolution of the lab experiment to the desired one, it can be seen in Table 2 that the desired resolution should be 74.54 times the resolution of the lab system:

$$\left.\frac{1}{dv}\right|_{desired} = \left.\frac{1}{dv}\right|_{lab} \cdot 74.54 \tag{53}$$

As a consequence, the ODVS parameters should be changed to obtain a higher ODVS resolution.

Mirror parameters are introduced by the Q factor, which is based on Eq. (51) as follows: Considering the solid angle to the mirror surface dS, the relation between the infinitesimal solid angles can be described by the following squared distance ratio, which will be denoted as the Q factor:

$$\frac{d\omega}{dv} = \left(\frac{d_v}{d_p}\right)^2 \triangleq Q \tag{54}$$

Expanding the ODVS resolution and substituting Eq. (54) gives:

$$\frac{1}{dv} = \frac{1}{dA}\frac{dA}{d\omega}\frac{d\omega}{dv} = \frac{1}{dA}\frac{dA}{d\omega}Q \tag{55}$$

Here, the resolution of the catadioptric camera equals the multiplicative-inverse pixel area $\frac{1}{dA}$, multiplied by the resolution of the camera $\frac{dA}{d\omega}$, and a function of the mirror parameters, represented by the factor Q. According to Eqs. (53) and (55), the desired resolution can be achieved by changing the pixel area, the conventional camera resolution, and the Q factor, to be 74.54 times larger than the lab system's values,

$$\left.\frac{1}{dv}\right|_{desired} = \left[\frac{1}{dA}\frac{dA}{d\omega}Q\right]_{desired} = \left[\frac{1}{dA}\frac{dA}{d\omega}Q\right]_{lab} \cdot 74.54 \tag{56}$$

The infinitesimal solid angle to the sensor $d\omega$, is given by dividing the projected pixel area dA, which is the infinitesimal sensor area, by the squared distance to the pixel. According to Fig. 16 it can be calculated by

$$d\omega = \frac{dA\cos\psi}{(\frac{f}{\cos\psi})^2} \tag{57}$$

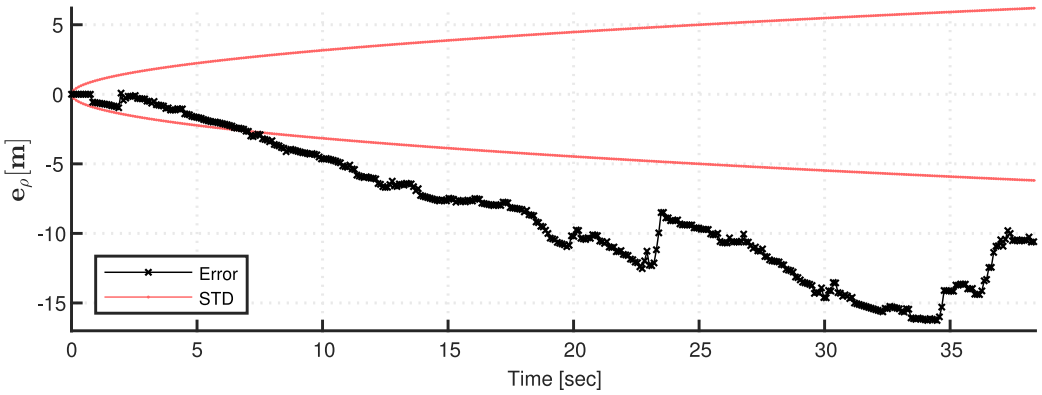

(a) ρ axis error.

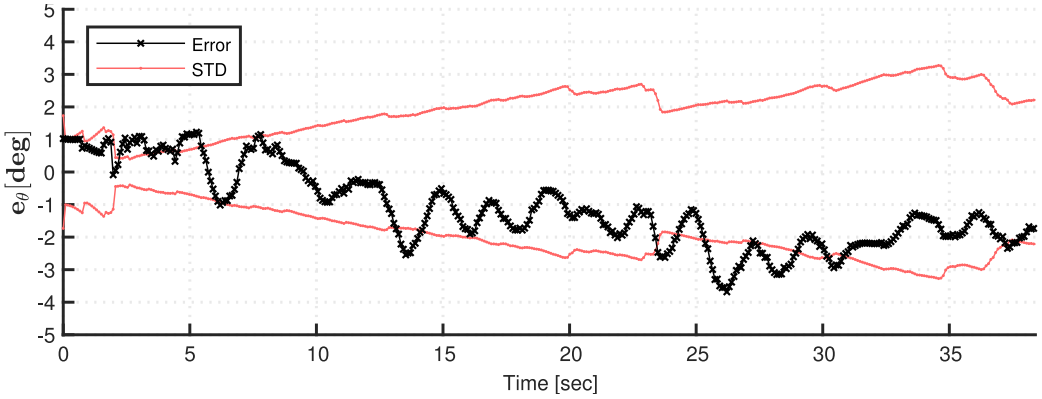

(b) θ axis error.

Fig. 14. Estimated relative state error, for the case of circular motion, represented by the spherical coordinate system, $\mathcal{S}$.

Table 1
Space scalability according to the first scenario.

Parameter	Units	Laboratory	Equivalent parameters (first scenario)
Target surface dimensions (w × h)	T_s [m^2]	$0.206 \times 0.042 = 8.652 \cdot 10^{-3}$	33.131
Target distance	d [m]	1.616	100
Number of target pixels	T_p [pixels]	90	90
Infinitesimal target area	dT [$\frac{\text{m}^2}{\text{pixel}}$]	$9.613 \cdot 10^{-5}$	0.3681
Infinitesimal solid angle to target	$d\nu$ [sr]	$3.681 \cdot 10^{-5}$	$3.681 \cdot 10^{-5}$

Table 2
Space scalability according to the second scenario.

Parameter	Units	Laboratory	Space desired (second scenario)
Target surface dimensions (w × h)	T_s [m^2]	$0.206 \times 0.042 = 8.652 \cdot 10^{-3}$	1
Target distance	d [m]	1.616	150
Number of target pixels	T_p [pixels]	90	90
Infinitesimal target area	dT [$\frac{\text{m}^2}{\text{pixel}}$]	$9.613 \cdot 10^{-5}$	0.0111
Infinitesimal solid angle to target	$d\nu$ [sr]	$3.681 \cdot 10^{-5}$	$4.938 \cdot 10^{-7}$
Resolution of ODVS	$\frac{1}{d\nu}$ [$\frac{1}{\text{sr}}$]	27166.53	Desired: $2.025 \cdot 10^6$ Obtained: $2.222 \cdot 10^6$
Sensor dimensions (w × h)	A [mm^2]	6.784×5.427	36×24
Sensor diagonal size	D [mm]	8.687	43.266
Sensor resolution	A [pixels]	$640 \times 512 = 307680$	4096×2160 $= 8847360$
Conventional camera focal distance	f [mm]	1.0977	5.4885
Pixel area	dA [μm^2]	10.6^2	8.79^2
Mirror focal distance	$2c$ [mm]	136.547	91.031
Crop Factor	CF		$\approx$5
Pixel Factor	PF		1.2059
Mirror Focal Distance Factor	MFDF		1.5

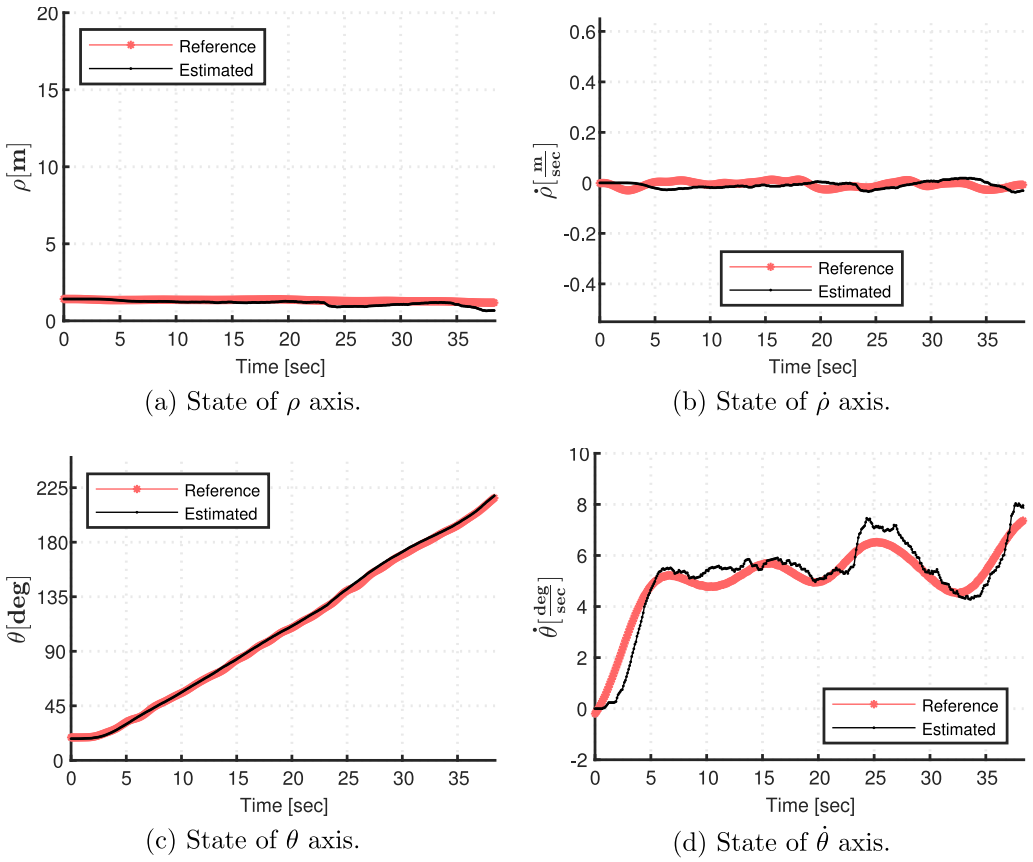

Fig. 15. Estimated relative state, for the case of circular motion and calibrated Extended Kalman Filter, represented by the spherical coordinate system, S.

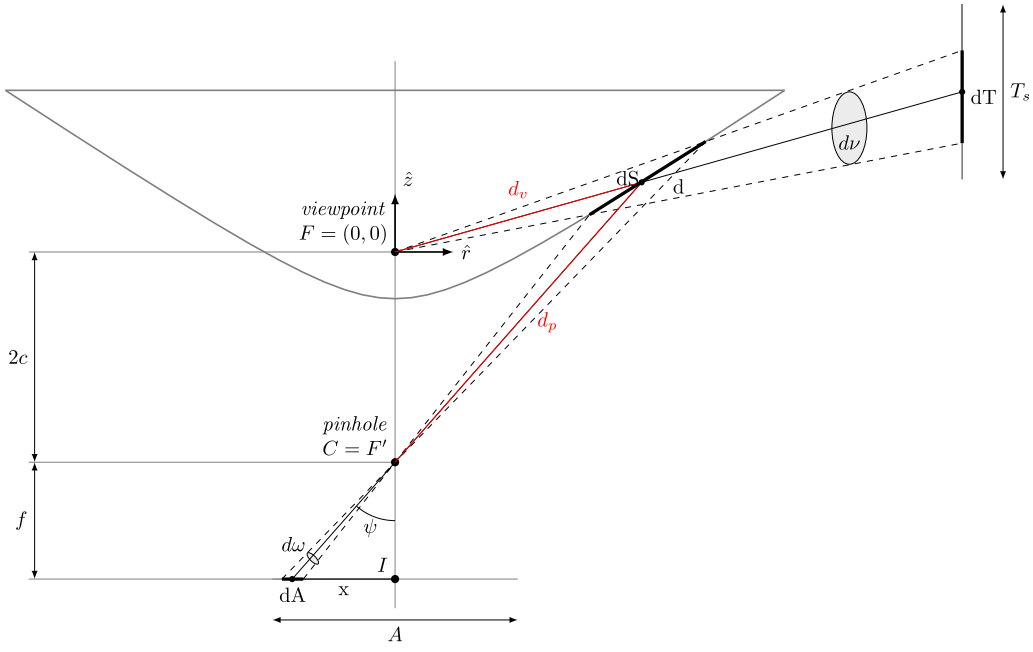

Fig. 16. Resolution analysis of a catadioptric camera with a hyperbolic mirror.

where f is the focal length and ψ is the angle between the optical axis and the line joining the pinhole to the center of the infinitesimal sensor area, dA. Based on Baker's analysis of ODVS resolution [9], conventional camera resolution is represented by the ratio between the infinitesimal sensor area dA, and the infinitesimal solid angle to the sensor $d\omega$. Rewriting Eq. (57), the conventional camera resolution is given by

$$\frac{dA}{d\omega} = \frac{f^2}{\cos^3 \psi} \tag{58}$$

For resolution calculations of the ODVS in the lab, calculate the conventional camera resolution first, according to Eq. (58). Here, ψ angle

is given by:

$$\psi = \arctan\left(\frac{x}{f}\right) \tag{59}$$

where f is the focal length, and x is the distance on the image sensor, between the infinitesimal sensor area dA and the optical axis. For the desired catadioptric camera, consider to use a full-frame format sensor for which the focal distance f is multiplied by the CF, which is given by the ratio between the sensors' diagonal size, D:

$$CF = \frac{D_{full-frame}}{D_{lab}} \tag{60}$$

The desired conventional camera resolution will be CF^2 times the lab conventional camera resolution, according to Eq. (58) and (59):

$$\left.\frac{dA}{d\omega}\right|_{desired} = \frac{f^2}{\cos^3\left[\arctan\left(\frac{x}{f}\right)\right]} \cdot CF^2 = \left.\frac{dA}{d\omega}\right|_{lab} \cdot CF^2 \tag{61}$$

The square root of the ratio between the pixel sizes will be referred to as a Pixel Factor (PF),

$$PF = \sqrt{\frac{dA_{lab}}{dA_{desired}}} = 1.2059 \tag{62}$$

Now we can write the multiplicative-inverse of the desired pixel size as

$$\left.\frac{1}{dA}\right|_{desired} = PF^2 \left.\frac{1}{dA}\right|_{lab} \tag{63}$$

Based on Fig. 16, the squared distance ratio of Eq. (54) can be expressed explicitly considering the frame $\mathcal{R}$, which is a Cylindrical right-hand body-fixed reference frame attached to the catadioptric camera's mirror viewpoint:

$$Q = \frac{d_v^2}{d_p^2} = \left[\frac{r^2 + z^2}{(2c + z)^2 + r^2}\right] \tag{64}$$

where r and z are the coordinates of the center of the mirror surface dS, expressed in the radial and axial axes respectively, and $2c$ is the distance between the focal points of the hyperboloid mirror. For the mirror parameter adjustment, using a mirror with smaller distance between the two focal points of the hyperboloid, will make the Q factor larger. To show this, we define a Mirror Focal Distance Factor (MFDF), which is the ratio between the focal distance of the mirror in the lab, $2c_{lab}$, and of the focal distance of the desired mirror, $2c_{desired}$.

$$MFDF = \frac{2c_{lab}}{2c_{desired}} \tag{65}$$

Next, we divide the focal distance of the lab mirror by $MFDF = 1.5$; this will make the Q factor 1.5^2 times larger according to Eq. (64). We assume that $2c_{lab} = 136.547$ mm is much larger than r and z of a peripheral point on the mirror ($r_{max}|_{lab} = 14$ mm, $z_{max}|_{lab} = 2.481$ mm).

$$\begin{aligned} Q|_{desired} &= \frac{r^2 + z^2}{(\frac{2c_{lab}}{MFDF} + z)^2 + r^2} \overset{2c_{lab} \gg r,z}{\approx} \frac{r^2 + z^2}{(2c_{lab} + z)^2 + r^2} \cdot MFDF^2 \\ &= Q|_{lab} \cdot MFDF^2 \end{aligned} \tag{66}$$

A smaller focal distance $2c$, can be achieved by keeping the same semiminor axis b, and a smaller semimajor axis a, according to the hyperboloid parameters relation:

$$c = \sqrt{a^2 + b^2} \tag{67}$$

Thus, the vertical FOV will be narrower, meaning a lower mirror shape.

Consequently, according to Eqs. (56), (61), (63) and (66), the obtained catadioptric camera resolution is

$$\left.\frac{1}{dv}\right|_{obtained} = \left.\frac{1}{dv}\right|_{lab} \cdot MFDF^2 \cdot PF^2 \cdot CF^2 \tag{68}$$

For the current scenario, $MFDF^2 \cdot PF^2 \cdot CF^2 = 81.798$, which is slightly larger than the desired ratio of 74.54. Hence, for a resolution equivalent to the lab experiment, and for desired target distance and size, a full-frame sensor with higher resolution and a lower hyperboloid mirror shape could be used.

5. Conclusions

This study shows that the spacecraft relative motion model bounds the growth of the non-observable depth, inherited from the ODVS. Additionally, this work compared between relative state estimation, based on measurements from a single ODVS, and fusion of sensors. Fusing ground station measurements improves the relative state estimation.

The experiments performed in the lab show that the relative state can be estimated, under the conditions of frictionless dynamics and visible target, using solely an ODVS. The non-observable depth effects, resulting from the monocular vision sensor, can be bounded using a good motion model and optimal filter tuning. The CV detection algorithms are shown to work properly with an ODVS, as well as at lab conditions, which resemble in some aspects the space conditions. Space scenarios possessing piecewise linear motion or circular motion dynamics, could be correlated to the corresponding experiments.

We conclude that an ODVS could be used as a tracking sensor for spacecraft relative navigation, when it is accompanied by another sensor, or by an accurate dynamical model. In various simulated scenarios, it has shown superiority to other vision sensors by its ability to observe the whole scene without the need to maneuver.

Declaration of competing interest

The authors declare that they have no known competing financial interests or personal relationships that could have appeared to influence the work reported in this paper.

References

[1] K. Alfriend, S. Vadali, P. Gurfil, J. How, L. Breger, Spacecraft Formation Flying: Dynamics, Control, and Navigation, first ed., Elsevier/Butterworth-Heinemann, 2009.

[2] Major Daniel D., Wright III, Counterspace Operations, Tech. rep, United States Air Force, 2004, URL https://fas.org/irp/doddir/usaf/afdd2_2-1.pdf.

[3] H. Schaub, L.E. Jasper, P.V. Anderson, D.S. McKnight, Cost and risk assessment for spacecraft operation decisions caused by the space debris environment, Acta Astronaut. 113 (2015) 66–79, http://dx.doi.org/10.1016/j.actaastro.2015.03.028.

[4] M. Lichter, S. Dubowsky, State, shape, and parameter estimation of space objects from range images, in: IEEE Int. Conf. Robot. Autom. 2004. Proceedings, Vol. 3, ICRA '04. 2004, IEEE, 2004, pp. 2974–2979, http://dx.doi.org/10.1109/ROBOT.2004.1307513.

[5] S. Segal, A. Carmi, P. Gurfil, Stereovision-based estimation of relative dynamics between noncooperative satellites: Theory and experiments, IEEE Trans. Control Syst. Technol. 22 (2) (2014) 568–584, http://dx.doi.org/10.1109/TCST.2013.2255288.

[6] T. Sogo, H. Ishiguro, M. Trivedi, Real-time target localization and tracking by N-ocular stereo, in: Proc. IEEE Work. Omnidirectional Vis. (Cat. No.PR00704), IEEE Comput. Soc., 2000, pp. 153–160, http://dx.doi.org/10.1109/OMNVIS.2000.853823.

[7] D.W. Rees, Panoramic television viewing system, 1967, URL https://patents.google.com/patent/US3505465A/en.

[8] S.K. Nayar, S. Baker, Catadioptric image formation, in: Proc. 1997 DARPA Image Underst. Work., New York, 1997, pp. 1431–1437.

[9] S. Baker, S. Nayar, A theory of catadioptric image formation, in: Sixth Int. Conf. Comput. Vis. (IEEE Cat. No.98CH36271), Narosa Publishing House, 1998, pp. 35–42, http://dx.doi.org/10.1109/ICCV.1998.710698.

[10] T. Svoboda, T. Pajdla, Epipolar geometry for central catadioptric cameras, Int. J. Comput. Vis. 49 (1) (2002) 23–37.

[11] L. Puig, J. Bermúdez, P. Sturm, J. Guerrero, Calibration of omnidirectional cameras in practice: A comparison of methods, Comput. Vis. Image Underst. 116 (1) (2012) 120–137, http://dx.doi.org/10.1016/j.cviu.2011.08.003.

[12] C. Geyer, K. Daniilidis, A Unifying Theory for Central Panoramic Systems and Practical Implications, in: ECCV 2000. Lect. Notes Comput. Sci., vol. 1843, Springer, Berlin, Heidelberg, 2000, pp. 445–461, http://dx.doi.org/10.1007/3-540-45053-X_29.

[13] J. Barreto, H. Araujo, Issues on the geometry of central catadioptric image formation, in: Proc. 2001 IEEE Comput. Soc. Conf. Comput. Vis. Pattern Recognition. CVPR 2001, Vol. 2, IEEE Comput. Soc., 2001, pp. II–422–II–427, http://dx.doi.org/10.1109/CVPR.2001.990992.

[14] C. Mei, P. Rives, Single view point omnidirectional camera calibration from planar grids, in: Proc. 2007 IEEE Int. Conf. Robot. Autom., IEEE, 2007, pp. 3945–3950, http://dx.doi.org/10.1109/ROBOT.2007.364084.

[15] T. Svoboda, T. Pajdla, V. Hlavač, Central panoramic cameras: design and geometry, in: Proc. Comput. Vis. winter Work. Gozd Martuljek, Slov. 1998.
[16] O. Tahri, H. Araujo, Non-central catadioptric cameras visual servoing for mobile robots using a radial camera model, in: 2012 IEEE/RSJ Int. Conf. Intell. Robot. Syst., IEEE, 2012, pp. 1683–1688, http://dx.doi.org/10.1109/IROS.2012.6385668.
[17] A. Voigtländer, S. Lange, M. Lauer, M. Riedmiller, Real-time 3D ball recognition using perspective and catadioptric cameras, in: Proc. 3rd Eur. Conf. Mob. Robot., EMCR 2007, University of Osnabruck, Germany, Freiburg, 2007, pp. 1–6.
[18] T. Ehlgen, T. Pajdla, D. Ammon, Eliminating blind spots for assisted driving, IEEE Trans. Intell. Transp. Syst. 9 (4) (2008) 657–665, http://dx.doi.org/10.1109/TITS.2008.2006815.
[19] D. Scaramuzza, R. Siegwart, Appearance-guided monocular omnidirectional visual odometry for outdoor ground vehicles, IEEE Trans. Robot. 24 (5) (2008) 1015–1026, http://dx.doi.org/10.1109/TRO.2008.2004490.
[20] A. Rituerto, L. Puig, J. Guerrero, Visual SLAM with an omnidirectional camera, in: 2010 20th Int. Conf. Pattern Recognit., IEEE, 2010, pp. 348–351, http://dx.doi.org/10.1109/ICPR.2010.94.
[21] G. Scotti, L. Marcenaro, C. Coelho, F. Selvaggi, C. Regazzoni, Dual camera intelligent sensor for high definition 360 degrees surveillance, IEE Proc. - Vis. Image Signal Process. 152 (2) (2005) 250, http://dx.doi.org/10.1049/ip-vis:20041302.
[22] J. Chahl, M. Srinivasan, A complete panoramic vision system, incorporating imaging, ranging, and three dimensional navigation, in: Proc. IEEE Work. Omnidirectional Vis. (Cat. No.PR00704), IEEE Comput. Soc., 2000, pp. 104–111, http://dx.doi.org/10.1109/OMNVIS.2000.853815.
[23] M. Lhuillier, Toward flexible 3D modeling using a catadioptric camera, in: 2007 IEEE Conf. Comput. Vis. Pattern Recognit., IEEE, 2007, pp. 1–8, http://dx.doi.org/10.1109/CVPR.2007.383164.
[24] A. Das, R. Fierro, V. Kumar, J. Ostrowski, J. Spletzer, C. Taylor, A vision-based formation control framework, IEEE Trans. Robot. Autom. 18 (5) (2002) 813–825, http://dx.doi.org/10.1109/TRA.2002.803463.
[25] A. Yilmaz, O. Javed, M. Shah, Object tracking, ACM Comput. Surv. 38 (4) (2006) 13, http://dx.doi.org/10.1145/1177352.1177355.
[26] T.-H. Chao, H. Zhou, G.F. Reyes, Spacecraft navigation using a grayscale optical correlator, in: D.P. Casasent, T.-H. Chao (Eds.), Optical Pattern Recognition XIII, Vol. 4734, SPIE, 2002, pp. 108–112, http://dx.doi.org/10.1117/12.458405.
[27] Y. Zhang, G. Feng, R. Xue, P. Yan, Study to real-time target recognizing system based on optical correlator, in: X. Hou, W. Zhao, B. Yao (Eds.), 27th International Congress on High-Speed Photography and Photonics, Vol. 6279, SPIE, 2007, http://dx.doi.org/10.1117/12.725342.
[28] M. Isard, A. Blake, Contour Tracking By Stochastic Propagation of Conditional Density, in: ECCV 1996. Lect. Notes Comput. Sci., vol. 1064, Springer, Berlin, Heidelberg, 1996, pp. 343–356, http://dx.doi.org/10.1007/BFb0015549.
[29] A. Lipton, H. Fujiyoshi, R. Patil, Moving target classification and tracking from real-time video, in: Proc. Fourth IEEE Work. Appl. Comput. Vision. WACV'98 (Cat. No.98EX201), IEEE Comput. Soc., 1998, pp. 8–14, http://dx.doi.org/10.1109/ACV.1998.732851.
[30] D.A. Vallado, W.D. McClain, Fundamentals of Astrodynamics and Applications, fourth ed., Microcosm Press, 2013.
[31] P. Zarchan, H. Musoff, Fundamentals of Kalman Filtering: A Practical Approach, Fourth Edition, fourth ed., American Institute of Aeronautics and Astronautics, Inc., Reston, VA, 2015, http://dx.doi.org/10.2514/4.102776.
[32] C. Mei, Laser-Augmented Omnidirectional Vision for 3D Localisation and Mapping (Ph.D. thesis), École nationale supérieure des mines de Paris, 2007.
[33] N. Otsu, A threshold selection method from gray-level histograms, IEEE Trans. Syst. Man. Cybern. 9 (1) (1979) 62–66, http://dx.doi.org/10.1109/TSMC.1979.4310076.
[34] Y. Oshman, I. Shaviv, Optimal tuning of a Kalman filter using genetic algorithms, in: AIAA Guid. Navig. Control Conf. Exhib., American Institute of Aeronautics and Astronautics, Denver, CO, 2000, http://dx.doi.org/10.2514/6.2000-4558.